Review

Recent Development in Vanadium Pentoxide and Carbon Hybrid Active Materials for Energy Storage Devices

Andrew Kim [1], Golap Kalita [2], Jong Hak Kim [3,*] and Rajkumar Patel [4,*]

1   Department of Chemical Engineering, The Cooper Union for the Advancement of Science and Art,
     New York, NY 10003, USA; kim70@cooper.edu
2   Department of Physical Science and Engineering, Nagoya Institute of Technology, Gokiso-Cho, Showa-ku,
     Nagoya 466-8555, Japan; golapkalita@gmail.com
3   Department of Chemical and Biomolecular Engineering, Yonsei University, 50, Yonsei-ro, Seodaemun-gu,
     Seoul 03722, Korea
4   Energy & Environmental Science and Engineering (EESE), Integrated Science and Engineering
     Division (ISED), Underwood International College, Yonsei University, 85 Songdogwahak-ro, Yeonsugu,
     Incheon 21983, Korea
*   Correspondence: jonghak@yonsei.ac.kr (J.H.K.); rajkumar@yonsei.ac.kr (R.P.)

Abstract: With the increasing energy demand for portable electronics, electric vehicles, and green energy storage solutions, the development of high-performance supercapacitors has been at the forefront of energy storage and conversion research. In the past decade, many scientific publications have been dedicated to designing hybrid electrode materials composed of vanadium pentoxide (V_2O_5) and carbon nanomaterials to bridge the gap in energy and power of traditional batteries and capacitors. V_2O_5 is a promising electrode material owing to its natural abundance, nontoxicity, and high capacitive potential. However, bulk V_2O_5 is limited by poor conductivity, low porosity, and dissolution during charge/discharge cycles. To overcome the limitations of V_2O_5, many researchers have incorporated common carbon nanostructures such as reduced graphene oxides, carbon nanotubes, carbon nanofibers, and other carbon moieties into V_2O_5. The carbon components facilitate electron mobility and act as porous templates for V_2O_5 nucleation with an enhanced surface area as well as interconnected surface morphology and structural stability. This review discusses the development of various V_2O_5/carbon hybrid materials, focusing on the effects of different synthesis methods, V_2O_5/carbon compositions, and physical treatment strategies on the structure and electrochemical performance of the composite material as promising supercapacitor electrodes.

Keywords: electrochemical energy storage; supercapacitor; vanadium pentoxide; carbon nanocomposite

1. Introduction

The demand for improved energy storage devices has increased due to the rapid development of portable electronics, electric vehicles, and green energy storage devices [1]. Supercapacitors are promising replacements for traditional energy storage devices such as batteries and capacitors with high energy and power densities, respectively, because supercapacitors can be fabricated using readily accessible materials with outstanding cyclability and can provide a balance of both high power and energy densities (Figure 1) [2–5]. The two main classifications of supercapacitors are electric double-layer capacitors (EDLCs) and pseudocapacitors (faradic supercapacitors) [6,7]. EDLCs produce a charge separation at the boundary between the electrode and electrolyte to store energy [8]. In contrast, pseudocapacitors rely on fast faradic reactions at the electrode surface to store energy [9]. Depending on the electrode material, supercapacitors primarily exhibit electric double-layer (EDL) or pseudocapacitive characteristics or a combination of both.
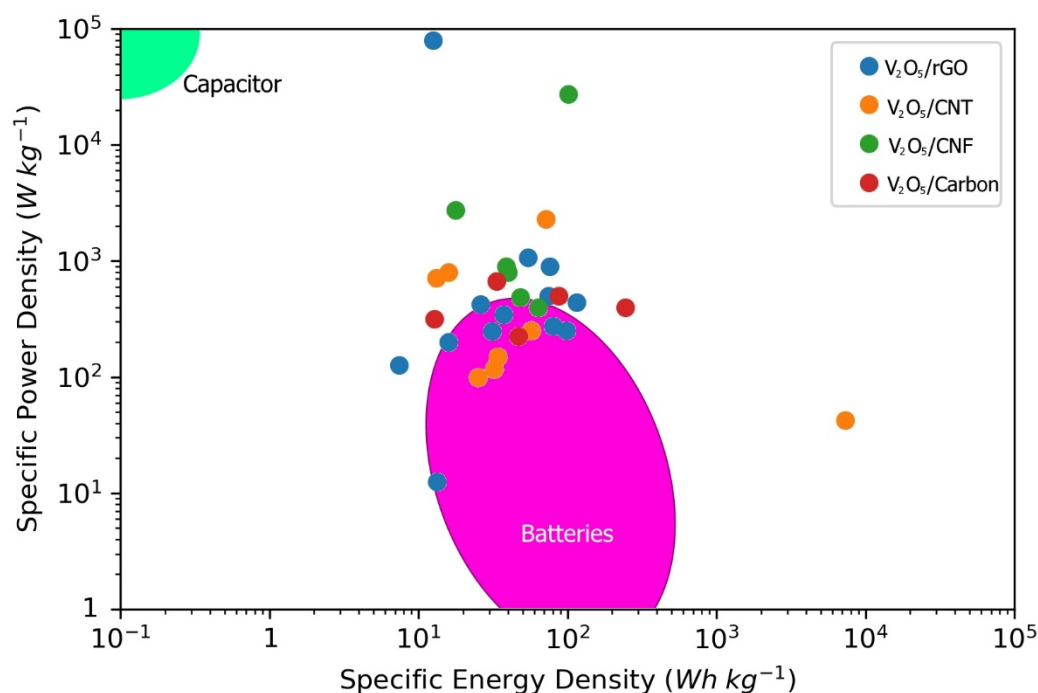
Figure 1. Ragone plot showing the energy and power density ranges of common electrochemical energy storage devices such as capacitors, supercapacitors, and batteries.

Transition metal oxide/carbon hybrid materials have recently attracted considerable attention as composites with easily controllable pseudocapacitive and EDL characteristics. Transition metal oxides such as vanadium pentoxide (V_2O_5) are pseudocapacitive, yielding supercapacitors with high specific capacitances (C_{sp}) and energy densities [10]. However, V_2O_5 is limited by poor conductivity, low power density, and minimal cyclic stability [11]. In contrast, carbon nanostructures, such as reduced graphene oxide (rGO), carbon nanotubes (CNTs), and carbon nanofibers (CNFs), show dominant EDL characteristics, resulting in highly stable and power-dense supercapacitors. However, carbon-based materials suffer from low specific capacitances and energy densities [12]. Transition metal oxide/carbon composite materials supplement the high energy potential of transition metal oxides with the high power potential and stability of carbon nanostructures [13–15]. These composite materials will be essential to meet the demand for fast-charging portable electronics, long-lasting electric vehicles, and environmentally friendly energy storage devices.

V_2O_5 has attracted significant attention as a transition metal oxide with multiple oxidation states (II–V), enabling a high maximum theoretical capacitance of 2120 F g^{-1} [16]. With a wide effective potential window, V_2O_5 can provide a high theoretical energy density [17]. Additionally, owing to its natural abundance and low toxicity, V_2O_5 is a low-cost material that is ideal for mass production [18,19]. The crystal structure of V_2O_5 allows electrolyte ions such as Li^+ to reversibly intercalate/de-intercalate, thereby improving the faradic reactivity with the electrolyte [20,21]. However, bulk V_2O_5 is limited by poor electrical conductivity, slow reaction kinetics, and vanadium dissolution [22,23]. To improve the properties of bulk V_2O_5, the bulk crystal nanostructure has been converted into nanorods [24], nanotubes [25], nanosheets [26], nanobelts [27], and other porous nanostructures [28]. These nanostructures allow better reaction kinetics with shorter diffusion pathways than those observed in the bulk crystal structure, and they improve cyclability with less strain on the crystal structure during ion intercalation/de-intercalation. However, these V_2O_5 materials still have drawbacks, such as low electrical conductivity [29,30].

Recent developments in improving V_2O_5 supercapacitor materials involve the addition of carbon nanomaterials, such as graphene [31], rGO [32], CNTs [33], and activated carbon (AC) [34], to improve the conductivity and structural stability of V_2O_5. Carbon materials are ideal sources of EDL capacitance for efficient supercapacitors, owing to high

porosities, conductivities, and natural abundances [35,36]. Highly porous carbon materials have large surface areas, resulting in more active sites on the electrode material [37]. Increased porosity allows fast ion intercalation/de-intercalation with short ion diffusion pathways [38]. The large surface area improves the interfacial contact between the electroactive material and the current collector, resulting in more efficient electron transfer. Moreover, the carbon content improves the overall conductivity of the electrode, increasing the specific capacitance and decreasing the energy losses during charge/discharge [39].

Despite the recent developments in V_2O_5/carbon composites, many review articles on supercapacitor electrode materials only briefly discuss V_2O_5 materials as part of a broader review of transition metal oxide [40–45] or carbon-based supercapacitors [46–48]. V_2O_5/carbon hybrid materials are promising materials that have been the focus of recent research, so it is essential to organize the most up-to-date information on factors affecting the performances of V_2O_5/carbon composite electrodes. This review describes the physical and electrochemical characteristics of different V_2O_5/carbon nanostructures, including V_2O_5/rGO, V_2O_5/CNTs, V_2O_5/CNFs, and other V_2O_5/carbon hybrid materials. This review focuses on the effects of different synthesis methods, carbon to V_2O_5 ratios, and physical treatment procedures on the structures and performances of V_2O and carbon hybrid nanomaterials.

2. V_2O_5/rGO

rGOs have been extensively investigated as additive materials for V_2O_5 composites because of their large surface areas, high conductivities, and good stabilities [49]. Similar to pristine graphene (sometimes reported in the literature as graphene), rGO is a monolayer of sp^2 hybridized carbon atoms arranged in a hexagonal lattice [50,51]. However, unlike pure graphene, rGO contains varying degrees of defects caused by functional groups such as hydroxyl and carbonyl groups remaining after the reduction of highly functionalized graphene oxide (GO) [52]. Various factors involved in the fabrication of a V_2O_5/rGO (VrG) electrode affect its electrochemical performance by altering the morphology and crystalline structure of the hybrid material. VrG composites are versatile materials that often possess a lamellar structure with high porosity and surface area. The effects of different synthesis pathways, V_2O_5/carbon compositions, and physical treatment conditions were closely examined for their impact on the nanostructures and the resulting capacitive performances of the VrG electrodes. The morphology and electrochemical performances of V_2O_5/rGO electrodes for supercapacitor applications reported in the literature are summarized in Table 1.

2.1. Effects of Synthesis Method

Many synthesis strategies for the fabrication of VrG composites include a hydro/solvothermal method. Typically, a mixture of V_2O_5 precursors such as vanadium oxytriisopropoxide (VTIP), rGO precursors such as GO, and water or other solvents are heated at high temperatures and pressures for extended periods in a Teflon-lined stainless steel autoclave [53]. The hydro/solvothermal procedure is frequently used because it is facile and allows the formation of diverse V_2O_5 morphologies on the 2D rGO substrate. Pandey et al. synthesized V_2O_5 nanospheres anchored to thin rGO sheets via a hydrothermal synthesis route. A uniform dispersion of VTIP, GO, isopropyl alcohol, and DI water was heated at 180 °C in an autoclave for 18 h, yielding a mesoporous VrG composite material [54]. The resulting material had a layered structure with large V_2O_5 nanospheres intercalated into the rGO layers. The vanadium crystals had an organized orthorhombic crystal structure that promoted deep ion adsorption. The lamellar structure of rGO increased the surface area for additional surface redox reactions and porosity for abundant electrolyte ion intercalation/de-intercalation. In a symmetric, two-electrode configuration with the VrG working electrodes, the composite exhibited a large maximum C_{sp} of 448 F g^{-1} at a current density of 0.75 A g^{-1} that decreased slightly to 296 F g^{-1} at a significantly higher current density of 15.5 A g^{-1}. The excellent rate capability was due to the low charge

transfer resistance (0.6 Ω), which was enabled by the strong bonds formed between the intercalated V_2O_5 nanospheres and conductive rGO sheets.

Table 1. V_2O_5 morphology and electrochemical performances of V_2O_5/reduced graphene oxide composite electrodes for supercapacitor applications.

Morphology	Maximum C_{sp} (F g^{-1})	Cycling C_{sp} Retention (%)	Cycle Number	Energy Density (Wh kg^{-1})	Power Density (W kg^{-1})
Nanowires	579	79	5000	-	-
Nanowires	710	95	20,000	98.6	250
Nanosheets	635	94 *	3000 *	75.9	900
Nanostrips	309	95.2	10,000	475	-
Amorphous	178.5	85	8000	13.3	12.5
Nanoflowers	1235	92	5000	116	440
Nanoribbons	-	720	500	16	200
Nanorods	37.2	90 *	1000 *	54.2	1075.9
Amorphous	484	83	1000	7.4	127
Amorphous	226	92	5000	12.5	79,900
Nanobelts	128.8	82	5000	-	-
Nanobelts	310.1	90.2 *	5000 *	31.3	249.7
Nanofibers	218	87 *	700 *	37.2	345
Nanowires	272	80	1000	26.22	425
Nanorods	537	84	1000	74.58	500
Nanospheres	386	-	-	80.4	275

* Cycling performance was determined using a two-electrode configuration.

The hydro/solvothermal synthesis route can also yield V_2O_5 nanowires. Ahirrao et al. followed a similar hydrothermal process with ammonium metavanadate (NH_4VO_3) to yield a similar lamellar rGO structure with intercalated V_2O_5 nanowires [55]. First, NH_4VO_3 was calcinated into V_2O_5, and the V_2O_5 powder was then sonicated with GO in DI water and heated at 180 °C for two days in an autoclave. The hydrothermal processes yielded thin nanowires with lengths ranging from 100 nm to several micrometers anchored to the rGO layers. The nanowire morphology increased the surface area of V_2O_5 for more active sites and decreased the ion diffusion pathways. The VrG composite was drop-cast onto carbon paper to yield a supercapacitor electrode. The VrG electrode exhibited a maximum C_{sp} of 1002 F g^{-1} at a current density of 1 A g^{-1}. Because of its low charge transfer resistance (0.53 Ω), the composite exhibited good rate capability, as indicated by the high C_{sp} of 828 F g^{-1} at a high current density of 3 A g^{-1}. Similarly, Geng et al. synthesized thin V_2O_5 nanowires anchored to curly rGO sheets using a hydrothermal process [56]. As the hydro/solvothermal process often yields a VrG composite powder, it is combined with a conducting filler and polymer binder and coated onto a current collector for use as an electrode. The VrG material was combined with Super P carbon (conducting filler), polyvinylidene fluoride (PVDF) (polymer binder), and N-methyl-2-pyrrolidone (NMP) (solvent) in an 8:1:1 ratio. The resulting slurry was coated onto Ni foam, vacuum dried, and compressed into a thin sheet. Unlike a 2D metal foil current collector, Ni foam provided a 3D macroporous network for large volumes of electrolyte diffusion. Anchoring the VrG material to the porous foam increased the surface area for more active redox sites. The electrochemical performance of the VrG hybrid material was tested in a three-electrode configuration with a VrG working electrode, Pt counter electrode, and Ag/AgCl reference electrode in 1 M KCl electrolyte. The Ni foam-based VrG electrode exhibited a high C_{sp} of 579 F g^{-1} at a current density of 1 A g^{-1}. Despite the lower conductivity than that of Cu, the relatively high conductivity and larger pore size of Ni foam enabled good rate capability, as indicated by a large C_{sp} of 534 F g^{-1} at a high current density of 4 A g^{-1}. Because of its rigid and porous structure, the VrG material was less susceptible to mechanical strain arising from electrolyte intercalation/de-intercalation, resulting in a high C_{sp} retention of 79% after 5000 cycles at a current density of 4 A g^{-1}. Sun et al. found that the duration of the hydro/solvothermal reaction affected the growth of V_2O_5 nanowires on rGO sheets [57].

V_2O_5 was modified with the N-doped rGO (N-rGO) aerogel via solvothermal synthesis in an autoclave at 160 °C for different durations. The composite was then freeze-dried to yield a marshmallow-shaped, free-standing VrG electrode. Tiny hair-like V_2O_5 nanowires were vertically anchored on the surfaces of the amorphous N-rGO sheets (Figure 2).
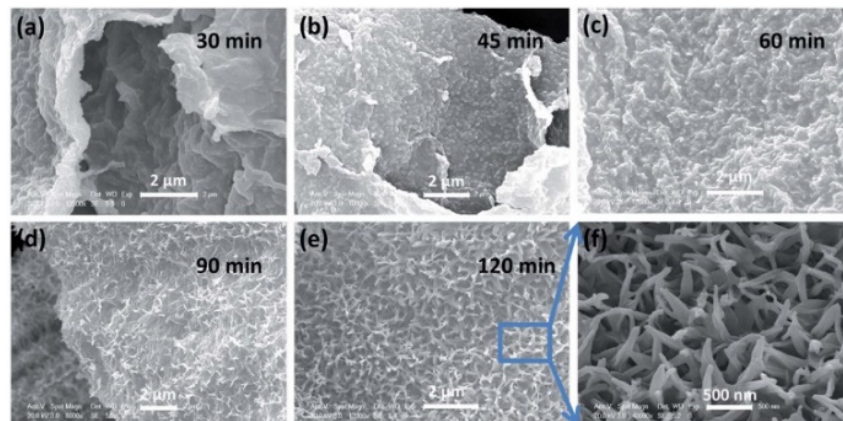

Figure 2. SEM images of N-doped rGO anchored to vertically aligned V_2O_5 nanowires after solvothermal synthesis for (**a**) 30, (**b**) 45, (**c**) 60, (**d**) 90, and (**e**) 120 min. (**f**) Magnified SEM image of the N-doped VrG after solvothermal reaction for 120 min. Reprinted with permission from Ref. [57]. Copyright 2018 Royal Society of Chemistry.

A short reaction time of 30 min between V_2O_5 and rGO resulted in a smooth rGO surface without many V_2O_5 nanowire growths (Figure 2a). After 45 to 60 min, larger V_2O_5 nanowires were obtained (Figure 2b,c), suggesting additional V_2O_5 nucleation and growth. Prolonged reactions for 90 to 120 min resulted in long, vertical V_2O_5 crystal growths uniformly spread on the rGO surface (Figure 2d,e). A magnified view of the V_2O_5 coated surface (Figure 2f) showed the porosity of vertically grown V_2O_5 nanowires. The mesoporous network of N-rGO sheets combined with the nanowire extrusions resulted in a large BET surface area of 416 $m^2\,g^{-1}$, which allowed fast ion diffusion and increased the number of active sites for surface reactions. The porous VrG electrode exhibited an excellent C_{sp} of 710 F g^{-1} at a current density of 0.5 A g^{-1}. The nitrogen defects in the rGO frame lowered the charge transfer resistance of the electrode from 1.54 to 1.11 Ω, resulting in improved rate capability, indicated by a high C_{sp} of 360 F g^{-1} at a large current density of 10 A g^{-1}. As the nitrogen groups in rGO were more reactive than carbon, N-rGO contained more V_2O_5 nucleation sites than bare rGO, resulting in denser distributions of V_2O_5 nanowires throughout the N-rGO-based composite. The V_2O_5/N-rGO material exhibited excellent cyclic stability with 95% C_{sp} retention after 20,000 cycles at a high current density of 10 A g^{-1}.

In addition to nanospheres and nanowires, the hydrothermal process can yield more sheet-like V_2O_5 morphologies anchored to rGO. Nagaraju et al. synthesized a VrG composite with V_2O_5 and rGO nanosheets via a hydrothermal method to obtain a lamellar composite structure [58]. V_2O_5 had a pure orthorhombic crystal structure that allowed good ion diffusion. The layered structure of the V_2O_5 and rGO nanosheets resulted in a large surface area of 36.2 $m^2\,g^{-1}$, which was four times larger than that of bulk V_2O_5. The VrG material exhibited both EDL and pseudocapacitive characteristics because of the even composition of V_2O_5 and rGO. The porosity and crystallinity enhanced the pseudocapacitive capability to a maximum C_{sp} of 635 F g^{-1} at a current density of 1 A g^{-1}. Even at a high current density of 30 A g^{-1}, the composite exhibited a large 240 F g^{-1} C_{sp}, highlighting the layered composite's potential for high-energy and high-power applications. An asymmetric supercapacitor with the VrG electrode exhibited an energy density of 75.9 Wh kg^{-1} with a power density of 900 W kg^{-1}. Sahu et al. used a hydrothermal method to synthesize V_2O_5 nanostrips anchored to rGO nanoribbon [59]. The V_2O_5 nanostrips shrank during the hydrothermal reaction with rGO as the rGO template inhibited large V_2O_5 growth. The

retention of small V_2O_5 crystals doubled the surface area to 15.6 m^2 g^{-1}, thereby increasing the efficiencies of surface redox reactions. The composite material had high mesoporosity, facilitating the fast diffusion of electrolytes through the ion channels. Thus, the C_{sp} of the composite (309 F g^{-1}) was approximately five times greater than that of bulk V_2O_5 nanostrips. The VrG material had a low equivalent series resistance and charge transfer resistance of 4.6 and 1.2 Ω, respectively, which provided good rate capability, indicated by the relatively high 114 F g^{-1} C_{sp} at a high scan rate of 100 mV s^{-1}. A solid-state electrode comprising the VrG composite exhibited a high conductivity of 1.4×10^{-2} S m^{-1}, which minimized the energy loss as heat. A symmetric VrG electrode supercapacitor had an energy density of 42.09 Wh kg^{-1} at a power density of 475 W kg^{-1}, which decreased to 13.44 Wh kg^{-1} at a power density of 8400 W kg^{-1}.

The facile hydrothermal method can also alter the large sheet-like structure of rGO. Zhang et al. employed a hydrothermal and freeze-drying procedure to fabricate a VrG hydrogel with thin rGO strips instead of large sheets [60]. The outer appearance of the hydrogel constituted a marshmallow-like macrostructure. The rGO strips were laced together to form a macroporous 3D structure. The V_2O_5 nanobelts were uniformly intercalated in the web-like rGO architecture. The VrG electrode with 64 wt% V_2O_5 exhibited a large C_{sp} of 320 F g^{-1} at a current density of 1.0 A g^{-1}. In a symmetric supercapacitor setup, VrG retained 70% of its initial C_{sp} after 1000 cycles at a current density of 1 A g^{-1}.

An alternative to the versatile hydrothermal process is the sol-gel method, which is a low-cost synthesis strategy that involves the formation of a V_2O_5 sol that is converted into a gel via hydrolysis and condensation reactions. The resulting porous V_2O_5 xerogel can be used as a free-standing, binderless material used directly as a supercapacitor electrode [61]. Yilmaz et al. utilized the sol-gel synthesis route to fabricate free-standing VrG electrodes [62]. The V_2O_5 gel was first synthesized via a hydrothermal process involving V_2O_5 powder and H_2O_2. The V_2O_5 gel, GO, and thiourea (cross-linking agent) were reacted for two weeks in a cylindrical glass vial. The resulting VrG aerogel was washed with ethanol, freeze-dried, and annealed at 300 °C in air. The highly porous composite had a large BET surface area of 83.4 g m^2 because of the lamellar rGO sheet structure with V_2O_5 nanoribbons anchored to the rGO surface. The addition of thiourea increased the chemical grafting between rGO and V_2O_5 by functioning as a redox couple, temporarily reducing V^{5+} to V^{4+} to initiate the polymerization between rGO and V_2O_5. The reduced V^{4+} was subsequently oxidized to V^{5+} during the final annealing step, yielding a hydrated orthorhombic V_2O_5 crystal structure. The symmetric supercapacitor with the thiourea-doped VrG electrodes exhibited a C_{sp} of 484.9 F g^{-1} at a current density of 0.6 A g^{-1}, which was twice that of a thiourea-less VrG. Using thiourea during the synthesis also resulted in sulfur and nitrogen functionalization of rGO. The functional groups decreased the equivalent series resistance to 1.6 Ω, resulting in good rate capability with a high C_{sp} of ~300 F g^{-1} at a high current density of 10 A g^{-1}. The mesoporous structure allowed high ion adsorption and decreased the mechanical strain during rapid ion intercalation/de-intercalation, resulting in a high C_{sp} retention of 80% after 10,000 cycles at a high current density of 5 A g^{-1}. A symmetric capacitor with the VrG xerogel electrodes possessed an energy density of 43.0 Wh kg^{-1} at a power density of 480 W kg^{-1}, which decreased to 24.2 Wh kg^{-1} at a power density of 9300 W kg^{-1}. Kiruthiga et al. also used the sol-gel method to synthesize V_2O_5 nanorods anchored to rGO sheets [63]. A V_2O_5 sol was prepared by reacting ammonium metavanadate with citric acid, and the sol was heated to form a gel that was subsequently heated at 450 °C in air to produce V_2O_5 powder. V_2O_5 was subsequently intercalated into the rGO sheets via sonication in DI water. The VrG composite exhibited a C_{sp} of 224 F g^{-1} at a current density of 0.01 A g^{-1} with a high C_{sp} retention of 85% after 1000 cycles at a current density of 0.06 A g^{-1}. An asymmetric Na-ion supercapacitor with a VrG anode and an AC cathode exhibited a maximum C_{sp} of 62 F g^{-1} at a current density of 0.01 A g^{-1} with 74% C_{sp} retention after 1000 cycles at a current density of 0.06 A g^{-1}. The supercapacitor produced a maximum energy density of 65 Wh kg^{-1} at a power density of 72 W kg^{-1} and a current density of 0.03 A g^{-1}.

Another method of synthesizing a VrG composite involves the filtration of an rGO and V_2O_5 suspension through a membrane. Unlike the hydrothermal method, the filtration process produces a stable and binderless thin-film electrode material. Wang et al. synthesized a VrG composite via the filtration of a solution of poly(3,4-ethylenedioxythiophene) (PEDOT), a conducting polymer, V_2O_5, and rGO through a cellulose acetate membrane [64]. The resulting binderless VrG thin film was then roll pressed onto various substrates such as ITO glass and Al to yield a substrate/PEDOT/VrG electrode. During synthesis, the V_2O_5 crystals were recrystallized into thin nanobelts coated evenly with PEDOT without the intercalation of the 3,4-ethylenedioxythiophene (EDOT) monomer into the V_2O_5 lattice. PEDOT acted as a bridge between V_2O_5 and rGO through π–π conjugation, such that V_2O_5 did not interact directly with rGO. These strong bonds allowed the composite material to form a stable film structure that was easily transferred to and compressed onto different substrates without a binder between the substrate and composite material. Figure 3a shows the procedure for transferring the thin-film hybrid material. A facile electrode fabrication procedure was applied to various substrates such as ITO, plastic, and glass. The VrG material exhibited smooth surface adhesion and good optical transparency for all tested substrates (Figure 3b,c). A large thin-film electrode with a diameter of 170 mm was easily fabricated (Figure 3d) and placed in an array (Figure 3e), demonstrating the viability of this fabrication strategy for scale-up. When placed on an Ag/PET current collector, the PEDOT/VrG electrode yielded an areal capacitance of 22.4 mF cm^{-2} at a current density of 0.7 A m^{-2}. A lack of binder between the substrate and PEDOT/VrG enabled direct contact between the conductive Ag substrate and composite material, increasing the overall electrochemical performance. The PEDOT coating on V_2O_5 reduced the dissolution of V_2O_5, resulting in a high capacitance retention of 98% after 150,000 cycles. Moreover, the outer rGO layer trapped the vanadium ions within the composite structure for maximum vanadium retention. A symmetric supercapacitor yielded a high C_{sp} retention of 92.4% after 50,000 cycles with a maximum energy density of 1800 Wh m^{-2} at a power density of 110,000 W m^{-2}. Similarly, Liu et al. synthesized a stable V_2O_5/rGO composite electrode via vacuum filtration through a cellulose acetate membrane [65]. A thin VrG film was fabricated by first preparing a lytropic liquid crystal suspension of rGO and V_2O_5 in DI water. The lamellar phase suspension was filtered through the cellulose membrane, yielding a VrG thin film that could withstand a maximum pressure of 120 MPa. With a 67 wt% V_2O_5, the thin film possessed a maximum C_{sp} of 205 F g^{-1} at a current density of 1 A g^{-1}. The electrode exhibited excellent rate capability by retaining more than 50% of its initial C_{sp} at a high current density of 50 A g^{-1}. The electrode retained 94% of its C_{sp} after 3000 cycles at a current density of 10 A g^{-1}. An added advantage of thin-film VrG materials is their high flexibility. Foo et al. utilized vacuum filtration through a nitrocellulose filter to synthesize a flexible VrG composite [66]. The VrG was peeled from the filter, heated in an autoclave with hydrazine monohydrate, dried, and acid-treated to yield a flexible, binderless VrG electrode. The hydrazine exfoliated the VrG into layers with an average spacing of 30 μm. Small amorphous V_2O_5 crystals were embedded on the surface of planar rGO layers. The thin-film material possessed a large Young's modulus of 1.7 GPa and tensile strength of 6.1 MPa and could be repeatedly bent and unbent around a test tube with no sign of permanent deformation. The flexible electrode material exhibited a C_{sp} of 178.5 F g^{-1} at a current density of 0.05 A g^{-1}. The hybrid thin film had a moderate rate capability due to a low equivalent series resistance of 3.36 Ω, resulting in a C_{sp} of 129.7 F g^{-1} at twice the current density. An asymmetric supercapacitor with a flexible VrG anode had maximum energy densities of 13.3 Wh kg^{-1} (unbent) and 13.6 Wh kg^{-1} (bent) at a power density of 12.5 W kg^{-1}.
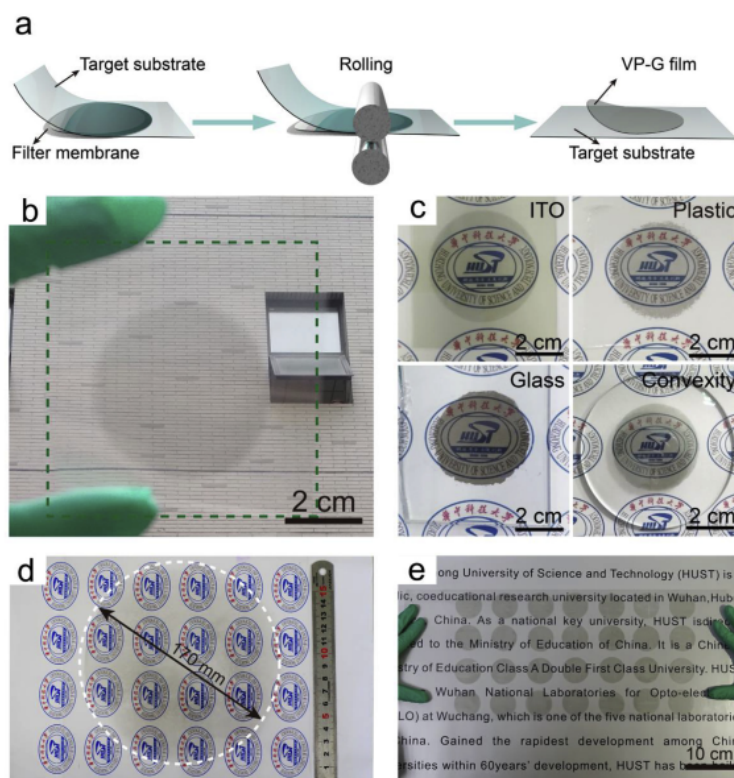
Figure 3. (**a**) Illustration of the transfer of the VrG film onto a substrate via a rolling process. Digital photographs of (**b**) transparent VrG films with a thickness of 22 nm, (**c**) transparent VrG on ITO, plastic, and glass with good convexity, and (**d**) a large VrG disc pressed on a substrate. (**e**) Digital photograph of a 7 × 4 array of the large-scale VrG films. Reprinted with permission from Ref. [64]. Copyright 2020 Elsevier.

Chemical deposition is a facile strategy for synthesizing a VrG composite directly on a conductive substrate. Different deposition techniques allow the composite material to bind to a well-structured, porous 3D network for structural stability and maximum porosity without the need for insulative additives or binders. Van Hoa et al. utilized chemical vapor deposition (CVD) to fabricate a free-standing graphene/V_2O_5 composite with a Ni foam template [67]. First, graphene was deposited on a Ni foam template using CVD, yielding a porous macrostructure with smooth graphene plates. Subsequently, V_2O_5 was deposited on the graphene/Ni foam substrate via a solvothermal method in an oxalic acid solution. The Ni foam was covered with uneven graphene plates after the initial CVD, increasing the surface area of the template. Small V_2O_5 nanoflowers were uniformly packed on the graphene surface. The flower-like nanostructures were intricately connected ultrathin V_2O_5 nanosheets with a highly orthorhombic crystal phase. The nanoflower extrusions on the porous graphene/Ni foam template further increased the BET surface area to 49.4 m^2 g^{-1} for increased redox reactions. As V_2O_5 was synthesized directly on the graphene/Ni foam template, there was no binder material to reduce the number of active sites. The electrode exhibited one of the highest reported C_{sp} values of 1235 F g^{-1} at a current density of 2 A g^{-1}. The direct contact between graphene and Ni foam resulted in high conductivity throughout the electrode material, resulting in a slight decrease in C_{sp} to 800 F g^{-1}, even at a large current density of 20 A g^{-1}. The large capacitance was due to the high specific surface area provided by the porous template and gaps between the petal-like V_2O_5. The composite electrode retained 92% of its C_{sp} after 5000 cycles at a high current density of 4 A g^{-1}, indicating good reversibility because of stable chemical bonding and enhanced conductivity. The energy density was 116 Wh kg^{-1} at a power density of 440 W kg^{-1}, which decreased to ~330 Wh kg^{-1} at a power density of ~3500 W kg^{-1}. Wang et al. employed a similar synthesis strategy to fabricate a Ni foam-based V_2O_5/rGO electrode [68]. HCl

and $FeCl_3$ were used to etch the Ni foam before graphene CVD to ensure strong, more homogeneously spread bonding. V_2O_5 was then synthesized directly on the rGO/Ni foam substrate via a solvothermal method in an ethanol solution, resulting in long V_2O_5 nanoribbons that were several micrometers in length. V_2O_5 was not completely oxidized and possessed a monoclinic crystal phase, while rGO showed a dominant graphitic crystal phase. The areal capacitance of the free-standing electrode was 822 mF cm^{-2} at a current density of 1 mA cm^{-2}. An asymmetric supercapacitor composed of a VG cathode had an energy density of 16 Wh kg^{-1} at a power density of 200 W kg^{-1}. Using chemical bath deposition (CBD) instead of CVD, Korkmaz et al. synthesized a binder-free, thin-film VrG [69]. Glass (G), poly(methyl methacrylate) (PMMA) (P), fluorine-doped tin oxide (FTO) glass (F), and indium tin oxide (ITO) glass (I) substrates were added to a solution of GO, $NaVO_3$, galactic acid, and methanol, and reacted for 24 h at ambient temperature. The coated substrate materials were removed via chemical blanket removal. The texture of the film surface differed for each substrate, showing spherical structures of different sizes for VrG-G, a smooth and homogeneous structure for VrG-P, a dense and grainy structure for VrG-F, and dispersed agglomerations for VrG-I. The crystallinity also changed depending on the substrate with amorphous, orthorhombic crystal growth observed in VrG-G and VrG-P, but well-oriented orthorhombic crystal growth in VrG-F and VrG-I. The thickness of the VrG film was also different, with values of 1025, 988, 689, and 393 nm for VrG-G, VrG-P, VrG-F, and VrG-I, respectively. Despite containing a thin V_2O_5 layer for limited pseudocapacitance potential, VrG-F exhibited the largest C_{sp} of 949.6 F g^{-1} owing to its organized crystalline structure.

Different synthesis strategies such as hydro/solvothermal, sol-gel, filtration, and chemical deposition methods are available for the preparation of VrG composites with varying V_2O_5 and rGO morphologies. The hydrothermal method is frequently used as a facile and versatile means of embedding V_2O_5 nanospheres, nanowires, nanorods, and nanosheets onto lamellar rGO sheets. The product is typically a VrG powder that must be combined with a conductive filler and binder for use as an electrode. The sol-gel method is an alternate process that yields a porous gel instead of a powder that can be directly applied as a supercapacitor electrode. The filtration method yields a thin-film, binderless electrode that can be physically transferred to different substrates such as ITO and plastic. Chemical deposition techniques such as CVD and CBD also allow the direct growth of V_2O_5 on porous and conductive substrates such as Ni foam and ITO for improved conductivity and stability.

2.2. Effects of Composition

Altering the ratio of rGO and V_2O_5 can improve the overall electrochemical performance by balancing the conductivity of rGO and the pseudocapacitance of V_2O_5. Li et al. emphasized the importance of carefully tuning the carbon content for improved electrochemical performance [70]. Different amounts of rGO were added during hydrothermal synthesis to yield VrG electrodes with 15, 22, and 26 wt% rGO. Even a relatively small difference of 4 wt% in the carbon content between VrG-22 and VrG-26 resulted in a significant increase in conductivity, with VrG-26 retaining 46% of its charge capacity (compared to 26% capacity retention of VrG-22) when the scan rate was increased from 1 to 20 mV s^{-1}. As the orthorhombic V_2O_5 nanorods were wrapped by and intercalated between the crumpled rGO sheets, an increase in the rGO content resulted in few nanorod agglomerations and high conductivity, resulting in improved rate capability. An asymmetric capacitor with a VrG-26 anode and AC cathode exhibited a C_{sp} of 37.2 F g^{-1} at a current density of 0.5 A g^{-1}. The integrated, layered structure of rGO reduced the permanent dissolution of V_2O_5, leading to 90% C_{sp} retention after 1000 cycles at a current density of 2 A g^{-1}. The maximum energy density exhibited was 54.3 Wh kg^{-1} at a power density of 136.4 W kg^{-1}. Saravanakumar et al. physically mixed different ratios of already prepared rGO and V_2O_5 in disodium citrate and aged the solution for three days to yield a VrG composite [71]. All VrG compositions had an orthorhombic V_2O_5 crystal structure and produced a complex

V_2O_5 network on the 2D rGO surface. However, among these, VrG-5 (5 wt% rGO) and VrG-15 (15 wt% rGO) resulted in more agglomeration of V_2O_5, whereas VrG-10 (10 wt% rGO) had a more homogeneous spread of the V_2O_5 crystals. V_2O_5 agglomeration limited surface ion adsorption as the electrolyte could not intercalate deep into the bulk V_2O_5 crystal structure. Thus, well-spread VrG-10 exhibited the highest C_{sp} of 519 F g^{-1} at a scan rate of 2 mV s^{-1}, which was significantly greater than the 326 F g^{-1} C_{sp} for pristine V_2O_5. An increase in rGO content improved the electron mobility to balance the high pseudocapacitive charge capacity of V_2O_5. VrG-15 performed worse than bare V_2O_5 with a C_{sp} of 210 F g^{-1} because of the lower V_2O_5 content and V_2O_5 agglomeration on rGO, which limited electron mobility and ion intercalation/de-intercalation. An increase in the rGO content enhanced the rate capability of the VrG electrodes, with VrG-5 showing only 47% C_{sp} retention compared to 68% retained by VrG-15 when the current density was increased from 0.5 to 10 A g^{-1}. Increasing the rGO content decreased the internal resistance, as indicated by 0.4 Ω resistance in VrG-10 compared to 1.73 Ω for pristine V_2O_5. The physical support provided by the rGO sheets further reduced the damage caused by repeated intercalation/de-intercalation, resulting in an 83% C_{sp} retention after 1000 cycles for VrG-10. An appropriate rGO composition is required to decrease V_2O_5 agglomeration for maximum pseudocapacitive efficiency and improve the conductive pathways for higher rate capability.

Although a high carbon content is desirable, a high V_2O_5 composition is required for energy-dense supercapacitor electrodes. Ramadoss et al. examined the effect of varying rGO to V_2O_5 ratio by controlling the initial ratio of GO and V_2O_5 during microwave synthesis [72]. All three VrG variations, V_1rG_2 (1:2 V_2O_5 to GO), V_1rG_1 (1:1 V_2O_5 to GO), and V_2rG_1 (2:1 V_2O_5 to GO), possessed a pure orthorhombic crystal phase with uniform nanorods of 150–200 nm lengths. The VrG electrodes exhibited mixed pseudocapacitive and EDL contributions to the overall capacitance. An increase in the V_2O_5 content increased the C_{sp} of the VrG electrode, as indicated by the higher C_{sp} of 250 F g^{-1} for V_2rG_1 than 103 F g^{-1} for V_1rG_2 at a scan rate of 5 mV s^{-1}. As V_2O_5 contributed toward most of the capacitance via faradic reactions, increasing the proportion of V_2O_5 increased the total capacitance. A symmetric supercapacitor with V_2rG_1 electrodes had an energy density of 12.5 Wh kg^{-1} at a power density of 79,900 W kg^{-1}, which decreased to 8.4 Wh kg^{-1} at 10 times the power density. Lee et al. also concluded that high V_2O_5 content increased the total capacitance [73]. VrG material was synthesized via a low-temperature hydrothermal process with different ratios of V_2O_5 powder and GO. V_3rG_1 (3:1 V_2O_5 to GO), V_1rG_1 (1:1 V_2O_5 to GO), and V_1rG_3 (1:3 V_2O_5 to GO) all yielded orthorhombic crystalline V_2O_5 nanobelts with uniform size. V_2O_5-rich V_3rG_1 outperformed the other two variations with a C_{sp} of 288 F g^{-1} at a scan rate of 10 mV s^{-1}, doubling the C_{sp} of V_1rG_3. Although an increase in the rGO content theoretically increased the conductivity, the low-temperature hydrothermal reduction led to only a partial reduction of GO to rGO, which limited the conversion to highly conductive rGO [73]. A large capacitance requires significant pseudocapacitive contributions, supporting the need for a V_2O_5-rich composite material. Many active sites were available for surface redox reactions because of the high surface area of the V_2O_5 nanobelts anchored to the rGO layers. However, excessive V_2O_5 content could lead to agglomeration that decreases the performance of the VrG composite. Fu et al. found a balance between the rGO and V_2O_5 contents by synthesizing VrG electrodes with different weight percentages of V_2O_5 [74]. The fabricated VrG composite synthesized via microwave synthesis method resulted in a uniform distribution of amorphous V_2O_5 nanoparticles on lamellar rGO sheets. Flaky rGO prevented the agglomeration of V_2O_5, which is a common problem that decreases the surface ion adsorption capability of the V_2O_5 nanostructure. More V_2O_5 crystals were formed on the rGO surface without agglomeration at a high initial V_2O_5 loading up to 34.1 wt%. VrG-34 (34.1 wt% V_2O_5) exhibited excellent electrochemical performance with a C_{sp} of 673.2 F g^{-1} at a current density of 1 A g^{-1}. The high rGO content resulted in high rate capability, as indicated by a large C_{sp} of 474.6 F g^{-1} at a high current density of 10 A g^{-1}. A high V_2O_5 composition decreased the ion adsorption and number

of interlayer rGO bridges, which are essential for fast electron transport. With an increase in current density, the high capacitance shifted from the redox dependence of V_2O_5 to the capacitive dependence provided by rGO. The porous and stable architecture of the composite allowed good cycling with a 96.8% C_{sp} retention after 10,000 cycles at a current density of 1 A g^{-1}. A symmetric supercapacitor exhibited good performance with an energy density of 46.8 Wh kg^{-1} at a power density of 499.4 W kg^{-1}. A high V_2O_5 content is necessary for high energy density through faradic energy storage; but ultimately, a balance between V_2O_5 and rGO is essential for maximizing the electrochemical performance.

A variation in the ratio of rGO to V_2O_5 also alters the porosity and surface area of the final VrG composite. Typically, a greater amount of rGO results in a larger surface area owing to its high surface area. Yao et al. found that decreasing V_2O_5 content increased the porosity of the composite [75]. A mixture of V_2O_5 powder with varying initial loading, H_2O_2, and GO sols was heated at 200 °C for 5 h to yield a VrG composite. The resulting VrG aerogel comprised V_2O_5 nanobelts with a pure orthorhombic crystal phase uniformly intercalated between the layers of rGO. VrG with 80.5 wt% V_2O_5 exhibited a small BET surface area of 20.5 m^2 g^{-1}, whereas VrG with 15.6 wt% V_2O_5 exhibited a large BET surface area of 103.4 m^2 g^{-1}. As rGO had a greater surface area than V_2O_5, the addition of higher amounts of rGO increased the overall surface area of the VrG material. Moreover, V_2O_5 tended to agglomerate at high concentrations. A decrease in the total V_2O_5 content resulted in a more homogeneous distribution of V_2O_5 throughout the rGO surface to provide more active sites. VrG-62 (61.6 wt% V_2O_5) outperformed other VrG electrodes owing to a good balance of EDLC and pseudocapacitance while maintaining a high pore volume of 0.008 cm^3 g^{-1}. The VrG-62 electrode exhibited a maximum C_{sp} of 310.1 F g^{-1} at a current density of 1 A g^{-1}. The VrG composite had good rate capability, as indicated by a high C_{sp} of 195.2 F g^{-1} at a large current density of 10 A g^{-1}. Choudhury et al. also reported that a lower V_2O_5 content of a V_2O_5/graphene (VG) composite increased the specific surface area [76]. The VG material was synthesized via an in situ chemical reaction between V_2O_5 powder and exfoliated graphene with H_2O_2. V_4G_1 (4:1 V_2O_5 to graphene) and V_2G_1 (2:1 V_2O_5 to graphene) exhibited a layered structure with V_2O_5 nanofibers anchored between the layers of rough graphene. The BET surface area of V_2G_1 was 142 m^2 g^{-1}, which decreased to 117 m^2 g^{-1} for V_4G_1. A low amount of V_2O_5 produced a composite with a high surface area, resulting in more active redox sites and greater intercalation/de-intercalation. Accordingly, V_2G_1 exhibited a higher C_{sp} of 218 F g^{-1} compared to 112 F g^{-1} for V_4G_1 at a current density of 1 A g^{-1}. A symmetric supercapacitor of V_2G_1 yielded an energy density of 22 Wh kg^{-1} at a power density of 3594 W kg^{-1}.

However, a balance between V_2O_5 and rGO could increase the surface area to greater than that of pure rGO. Deng et al. found that a VrG composite yielded higher porosity than that of pure rGO because of the increased interlayer spacing of the rGO sheets caused by V_2O_5 intercalation [77]. A VrG monolith was synthesized via a hydrothermal method, resulting in a lamellar rGO structure with V_2O_5 nanowires embedded between the thin rGO sheets (22 wt% rGO). The resulting BET surface area of the VrG monolith was 172.9 m^2 g^{-1}, which was ~100 m^2 g^{-1} larger than that of a pure rGO monolith and approximately five times larger than that of pure V_2O_5. The VrG monolith was also compressed into a thin film electrode. The C_{sp} of VrG monolith and thin-film were 385 and 272 F g^{-1}, respectively, at a current density of 0.25 A g^{-1}. The VrG material exhibited enhanced ion diffusion rates owing to increased porosity, resulting in good rate capability, as indicated by a high C_{sp} of 224 F g^{-1} at a current density of 10 A g^{-1}. The energy density of the asymmetric supercapacitor with the VrG electrode was 26.22 Wh kg^{-1} at a power density of 425 W kg^{-1}, which decreased to 7 Wh kg^{-1} at a power density of 8500 W kg^{-1}. Ndiaye found that an increase in the graphene foam (GF) content only increased the porosity to a certain extent [78]. A V_2O_5/GF composite was synthesized with varying initial GF loading. The BET surface area increased from 4.9 m^2 g^{-1} for pristine V_2O_5 nanosheets to 5.1 m^2 g^{-1} when 50 mg of GF was added. Because GF has a high specific surface area of 208.8 m^2 g^{-1}, the initial integration of GF increased the overall surface area. The low

GF content also prevented the homogeneous integration of the V_2O_5 nanosheets with GF. An increase in the GF loading to 150 mg (VrG-150) resulted in a maximum surface area of 9.5 m^2 g^{-1}. However, further increase in the GF loading to 200 mg resulted in the reduction of surface area to 6.2 m^2 g^{-1}. A high GF content caused GF and V_2O_5 to form separate agglomerations instead of a homogeneous composite. Consequently, the porous and homogeneous VrG-150 outperformed the other electrodes, with a specific capacity of 73 mAh g^{-1} at a current density of 1 A g^{-1}. An asymmetric capacitor assembled using a VrG-150 positive electrode and carbonized Fe-adsorbed polyaniline (C-FE-PANI) negative electrode yielded a specific capacity of 41 mAh g^{-1} at a current density of 1 A g^{-1}. The energy density was 39 W h kg^{-1} at a power density of 947 W kg^{-1}.

Determining the optimal ratio between rGO and V_2O_5 is essential for synthesizing a high-performance electrode material with a balance between the EDL and pseudo-capacitive characteristics. An appropriate rGO content improves the conductivity and electrode cyclability, whereas a sufficient V_2O_5 content is necessary for high specific capacitance. The addition of rGO to bulk V_2O_5 increases the surface area of the composite material, and the intercalation of V_2O_5 into rGO layers can also increase the porosity of the composite material. However, a balance between the two components is necessary to prevent agglomeration.

2.3. Effects of Physical Treatment

Annealing newly fabricated VrG composites can alter oxidation states of vanadium oxides and improve their crystallinity, resulting in enhanced electrochemical performance. Control of the temperature during the heat treatment can increase the oxidation of V_2O_5 and the formation of a homogeneous composite. Following a hydrothermal synthesis procedure, Li et al. synthesized V_xO_y nanoflowers anchored to rGO sheets [79]. Annealing of the resulting composite caused the nanoflowers to morph into V_2O_5 nanorods with varying lengths and diameters depending on the annealing temperature. Moreover, an increase in the annealing temperature converted amorphous vanadium oxides into orthorhombic V_2O_5 crystals through the oxidation of V^{4+} to V^{5+}. VrG annealed at 350 °C under nitrogen atmosphere exhibited the maximum C_{sp} of 537 F g^{-1} at a current density of 1 A g^{-1} due to short ion diffusion pathways in the organized V_2O_5 crystal lattice. Because the nanorods were uniformly anchored to the mesoporous rGO surface, the high conductivity and porosity afforded by the rGO resulted in a good rate capability, indicated by the 60% C_{sp} retention at a high current density of 20 A g^{-1}. Improved cyclic performance of the VrG material was also observed, with 84% C_{sp} retention after 1000 cycles at a current density of 1 A g^{-1}. The VrG electrode exhibited a high energy density of 74.58 Wh kg^{-1} at a power density of 500 W kg^{-1}, which decreased slightly to 29.33 Wh kg^{-1} at a power density of 10,000 W kg^{-1}. In a similar study, Liu et al. fabricated a VrG composite via a hydrothermal method using an NH_4VO_3 precursor followed by annealing at different temperatures in air [80]. Without annealing, V_2O_5 nanospheres of inconsistent sizes and incomplete formation were observed, whereas VrG annealed at a high temperature of 350 °C (VrG-350) exhibited a degraded rGO support without distinct V_2O_5 nanospheres. However, VrG annealed at 300 °C (VrG-300) had uniformly sized V_2O_5 nanospheres homogeneously embedded on the surface of the rGO. VrG-300 exhibited greater GO reduction and an increase in V_2O_5 composition from 12 to 30 wt%, owing to greater V^{4+} oxidation to V^{5+}. With fewer defects in the carbon lattice and a higher V_2O_5 content, VrG-300 exhibited the largest C_{sp} of 386 F g^{-1} at a current density of 0.5 A g^{-1}. An asymmetric supercapacitor with the VrG-300 electrode had a maximum energy density of 80.4 Wh kg^{-1} at a power density of 275 W kg^{-1}, which decreased to 32 Wh kg^{-1} at a power density of 1374 W kg^{-1}. Thangappan et al. electro-spun a mixture of vanadium acetylacetonate, GO, polyvinyl pyrrolidone, dimethylformamide (DMF), and ethanol, and subsequently annealed the composite at 350 or 550 °C in air [81]. Non-annealed VrG and VrG annealed at 350 °C resulted in a web of uniformly thin and straight nanowires. VrG annealed at 550 °C resulted in a twisted and aggregated structure with arched webs that were half the diameter of the

non-annealed VrG due to the decomposition of the organic binder material. Annealing at 550 °C completely reduced GO, resulting in a more conductive composite fiber. However, high temperature disintegrated the carbon material, resulting in a low carbon content of 0.3 wt%. Non-annealed and low-temperature annealed VrG had amorphous crystal structures, whereas the VrG annealed at 550 °C possessed an orthorhombic crystal structure, as indicated by the formation of large V_2O_5 crystals. The stable crystals and mesoporous, web-like structure of VrG annealed at 550 °C allowed a large amount of ion diffusion into the electrode for high energy storage. The C_{sp} was 453.8 F g^{-1} at a scan rate of 10 mV s^{-1} because of the slow ion intercalation at low scan rates. The C_{sp} decreased to 111.01 F g^{-1} at a scan rate of 100 mV s^{-1}. Therefore, the control of the annealing temperature is essential for both the reduction of GO to rGO and improving the crystallinity of V_2O_5.

Despite the previously mentioned benefits of heat treatment, the annealing of VrG electrodes may decrease the electrical performance. Lee et al. analyzed the discrepancy in the electrochemical performance of a non-annealed V_2O_5 composite in comparison with an annealed composite, where an rGO thin film was fabricated from GO using CO_2 laser reduction, and V_2O_5 was deposited on the film via atomic layer deposition [82]. The CO_2 laser changed the porosity of the compact GO by increasing the interstitial gap between the rGO sheets while creating pores that penetrated multiple rGO sheets. The spacing between the rGO sheets increased with V_2O_5 infiltration. The V_2O_5 deposition left the rGO template intact, and further annealing the composite in an argon atmosphere did not significantly change the surface morphology of the electrode. However, annealing converted the amorphous V_2O_5 crystal structure into a more crystalline V_2O_5 with varying oxidation states of vanadium oxide. The amorphous crystal characteristics of V_2O_5 before annealing allowed deeper ion diffusion through the distorted lattices, resulting in a greater faradic character. In contrast, the annealed VrG exhibited higher crystallinity and greater EDL contribution. Considering the lamellar structure of the rGO sheets, the diffusion-based faradic capacitance of the non-annealed VrG resulted in a higher C_{sp} of 189 F g^{-1} at a current density of 1 A g^{-1}. The charge transfer resistance was also lower for the non-annealed VrG. Initial cycling increased the C_{sp} to 108% for the non-annealed VrG material owing to electro-activation caused by the initial intercalation of electrolyte ions. However, this did not occur for annealed VrG because of the more rigid crystallized structure of the annealed VrG (Figure 4).

In addition to heat treatment, the morphology and crystallinity of a VrG composite can be altered by laser irradiation. Lazauskas et al. first synthesized a V_2O_5/GO nanoribbon composite using a melt-quenching process and further applied laser treatment to reduce GO to rGO [83]. A 405-nm laser was used to irradiate specific regions of the V_2O_5/GO composite, resulting in a VrG composite with surface protrusions. The laser treatment resulted in pillar-like V_2O_5 protrusions that uniformly extruded from the rGO base. These protrusions increased the surface area by four times to 17.27 m^2 g^{-1}. An increase in the laser power output from 1.69 to 2.03 W cm^{-2} to 2.37 W cm^{-2} resulted in more protrusions. However, further increase in power to 2.71 W cm^{-2} led to larger V_2O_5 agglomerations, thereby decreasing the surface area of the composite material. The laser treatment also decreased the amount of intercalated H_2O molecules in the V_2O_5 crystal lattice while further reducing GO to rGO. The laser treatment resulted in a VrG composite with a more organized V_2O_5 crystal structure and high conductivity of 6.8 S m^{-1}.

Physical treatment of V_2O_5 with heat or laser can alter the crystallinity of V_2O_5, oxidize V^{4+} to V^{5+} and reduce GO to rGO. Highly crystalline V_2O_5 is more conductive than amorphous V_2O_5, allowing for greater rate capability, but it is less efficient for ion diffusion than the latter. The reduction of GO to rGO improves the conductivity of the carbon backbone in the VrG composite. Physical treatment can also be used to control the formation of agglomerations, and excessive heat exposure can destroy the carbon content of the hybrid material.
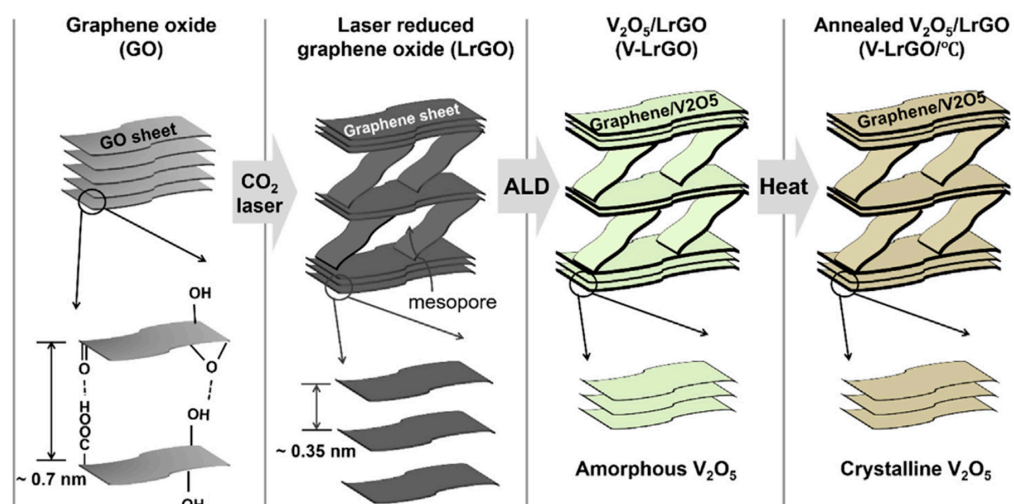
Figure 4. Schematic illustration for the fabrication process of the multilayered graphene (i.e., LrGO) and amorphous or crystalline V_2O_5 coated LrGO. Firstly, the prepared GO was reduced by a home engraver equipped with a CO_2 laser. Then, the LrGO was coated with amorphous V_2O_5 by a low-temperature ALD process, followed by annealing at high temperatures. Reprinted with permission from Ref. [82]. Copyright 2020 Elsevier.

3. V_2O_5/CNT

CNTs have received considerable attention owing to their high conductivities, large surface areas, mechanical stability, and unique 1D tubular structures [84,85]. The ability of CNTs to be functionalized allows precise control of their properties to meet the needs of specific supercapacitor applications [86]. Single-walled CNTs (SWCNTs) and multi-walled CNTs (MWCNTs) have been utilized in conjunction with vanadium oxides to yield high-performance hybrid materials for supercapacitor applications [87]. Herein, the effects of different synthesis pathways, V_2O_5/CNT compositions, and physical treatments on the morphology and electrochemical performances of V_2O_5/CNT (VCNT) composite materials are discussed. The morphology and electrochemical performances of V_2O_5/CNT electrodes for supercapacitor applications reported in the literature are summarized in Table 2.

Table 2. V_2O_5 morphology and electrochemical performances of V_2O_5/carbon nanotube composite electrodes for supercapacitor applications.

Morphology	Maximum C_{sp} (F g^{-1})	Cycling C_{sp} Retention (%)	Cycle Number	Energy Density (Wh kg^{-1})	Power Density (W kg^{-1})
Nanostars	1016	64 *	5000 *	13.24	710
Nanospheres	125	-	400	25	100
Nanobelts	685	99.7	10,000	34.3	150
Amorphous	410	86	600	57	250
Nanoflakes	629	93	4000	72	2300
Nanosheets	207.7	75 *	10,000 *	7300	42.6
Nanospheres	284	76 *	5000 *	32.3	118
Nanosheets	357.5	99.5	1000	-	-
CNT Coating	510	96	5000	16	800

* Cycling performance was determined using a two-electrode configuration.

3.1. Effects of Synthesis Method

A common procedure for fabricating VCNT composites is the hydro/solvothermal method. Jiang et al. grew V_2O_5 crystals on a GF/CNT substrate by employing a hydrothermal process [88]. Subsequently, PEDOT coating was deposited via a chronoamperometry technique, yielding a VCNT/GF/PEDOT composite (Figure 5).
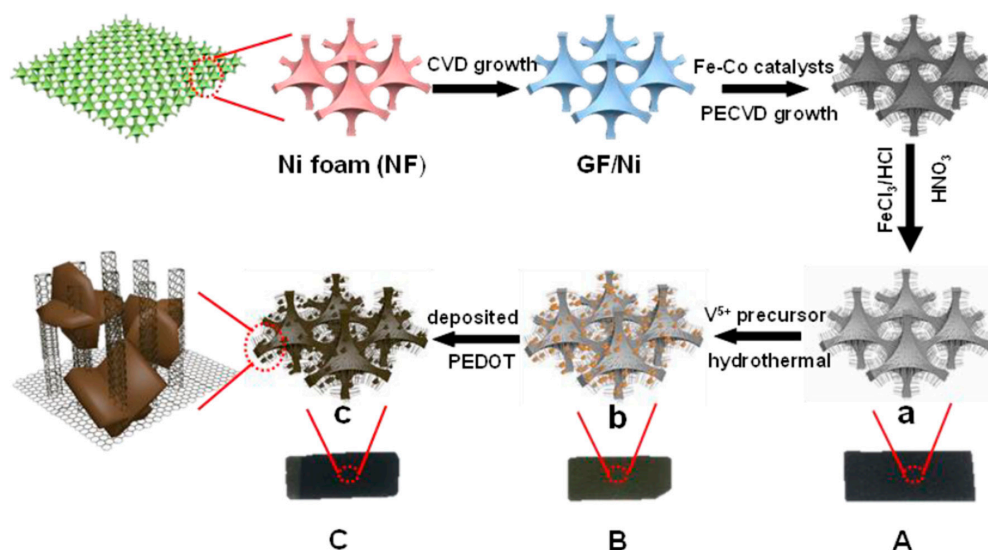
Figure 5. Schematic of the synthesis of (**A**) CNT/GF, (**B**) VCNT/GF, (**C**) VCNT/GF/PEDOT. Reprinted with permission from Ref. [88]. Copyright 2017 Royal Society of Chemistry.

Orthorhombic crystal phase V_2O_5 nanostars were intercalated into the interstitial space between the vertically aligned CNTs. The addition of the PEDOT coating reduced the V_2O_5 dissolution during synthesis and increased the size of the V_2O_5 nanostars by ~15%. The high surface area of the enlarged V_2O_5 nanostars increased the pseudocapacitive surface reactions. The composite electrode was tested in a three-electrode configuration with a Pt counter electrode and an Ag/AgCl reference electrode in 5 M $LiNO_3$ electrolyte, yielding a high C_{sp} of 1016 F g^{-1} at a current density of 1 A g^{-1}. The direct growth of V_2O_5 on the vertically aligned CNTs enabled good surface contact for efficient electrical conduction. The porous Ni foam/CNT frame also provided structural stability to the overall electrode. The result indicated good rate capability with an excellent C_{sp} of 484 F g^{-1} at a high current density of 20 A g^{-1} and high coulombic efficiency of 97.8%. The asymmetric supercapacitor with a VCNT electrode exhibited a maximum energy density of 13.24 Wh kg^{-1} at a power density of 710 W kg^{-1}, which decreased to 10.34 Wh kg^{-1} at a power density of 2659 W kg^{-1}. The energy density decreased slightly at high power owing to the absence of an insulating binder material and the high conductivity provided by the Ni/CNT frame. Wang et al. synthesized a VCNT composite by adding CNTs to the V_2O_5 nanosheets that were synthesized via a hydrothermal reaction between bulk V_2O_5 and H_2O [89]. CNTs were subsequently added to a solution of V_2O_5 nanosheets and aged for two days. This fabrication method resulted in a lamellar nanostructure with V_2O_5 layers intercalated with CNTs, corresponding to 13.7 wt% of the total composition. The CNTs increased the interstitial spacing between the V_2O_5 nanosheets, preventing V_2O_5 agglomeration and increasing the porosity, yielding a large specific surface area of 102.05 m^2 g^{-1}. The C_{sp} of the VCNTs was 553.33 F g^{-1} at a current density of 5 mA cm^{-2}. The increased interlayer spacing between the V_2O_5 planes allowed greater ion intercalation/de-intercalation, which promoted faradic redox reactions. Furthermore, the CNTs increased the overall conductivity of the device, resulting in a low series resistance of 0.95 Ω and a charge transfer resistance of 0.6 Ω for enhanced rate capability. Owing to the structural stability provided by the CNTs, the charge/discharge stability increased, as indicated by a high C_{sp} retention of 83% after 1000 cycles at a current density of 10 mA cm^{-2}.

Deposition techniques have also been used to grow vertically aligned CNTs and V_2O_5 composites directly on conductive substrates such as Ni, yielding a binderless electrode material. Jampani et al. used CVD to synthesize an array of vertically aligned CNTs on flat Ni disks that formed a forest-like microstructure. Atmospheric pressure CVD was used to deposit Ti-doped V_2O_5 on the CNTs [90]. The resulting composite had an amorphous

crystal phase with V_2O_5 globules anchored to the vertically aligned CNT forest; a C_{sp} of 313 F g^{-1} was observed at a scan rate of 2 mV s^{-1}. The amorphous crystal structure of the Ti-doped V_2O_5 decreased the V_2O_5 dissolution during charge/discharge, resulting in nearly perfect C_{sp} retention even after 400 cycles at a high scan rate of 100 mV s^{-1}. The areal capacitance was 350 mF cm^{-2} at a scan rate of 2 mV s^{-1}, which decreased to 20 mF cm^{-2} at a scan rate of 200 mV s^{-1}. The decent rate capability was due to the low resistance of the binderless composite at 0.0182 Ω cm^2, which was two orders of magnitude more conductive than pristine V_2O_5. The electrodes had a maximum energy density of 25 Wh kg^{-1} at a power density of 100 W kg^{-1}, which decreased to 11 Wh kg^{-1} at a power density of 4500 W kg^{-1}. Shakir et al. used spray coating to prepare a layered V_2O_5/MWCNT (VMWCNT) composite electrode on a Ni/Cu/Ni/Au electroplated substrate [91]. A polyester fiber fabric was first plated with Ni/Cu/Ni/Au layers sequentially via electroless plating. The MWCNT/V_2O_5 core/shell nanotubes were synthesized via a bottom-up assembly method using pre-functionalized MWCNTs and NH_4VO_3. A layer of graphene was then deposited on the conductive fabric. Subsequently, a mixture of V_2O_5-coated MWCNTs was spray-coated on the top graphene layer. Alternating graphene and VMWCNT layers were applied repeatedly to yield a binderless VMWCNT/graphene composite electrode. The electrode comprised a thick orthorhombic V_2O_5 shell coating the MWCNTs. The C_{sp} of the VMWCNT/graphene electrode with 3-nm-thick V_2O_5 layers had an excellent C_{sp} of 2590 F g^{-1} at a scan rate of 1 mV s^{-1}. Increasing the V_2O_5 coating thickness to 20 nm decreased the C_{sp} to 510 F g^{-1} because of inefficient ion penetration into the inner layers of the VMWCNTs. The 3-nm-thick VMWCNT/graphene electrode retained 96% of its initial C_{sp} after 5000 cycles at a scan rate of 20 mV s^{-1} because of the effective conductive MWCNT bridge linking electron transport from V_2O_5 to graphene. The energy density was 96 Wh kg^{-1} at a power density of 800 W kg^{-1}, which decreased to 28 Wh kg^{-1} at a power density of 9000 W kg^{-1}.

One major advantage of CNTs is their easy functionalization to yield high-performance VCNT electrodes through various synthesis methods. Modifying CNTs with specific functional groups such as hydroxyl or carboxyl groups can improve the conductivity of the CNTs and promote the nucleation of V_2O_5 crystals. Hu et al. used a one-step hydrothermal method to synthesize a vanadium oxide composite with functionalized CNTs [92]. The CNTs were functionalized with hydroxyl and carbonyl groups using concentrated sulfuric and nitric acids, which acted as the activation centers for coordinate bond formation with VO. Vanadium oxide nanoribbons were formed at the nucleation sites via a hydrothermal reaction and were bonded to the CNTs via hydroxyl functional groups. By adding GO to a mixture of V_2O_5 and CNTs, Hu et al. fabricated a V_3O_7/CNT/rGO composite (rGO-VCNT) comprised of rGO sheets uniformly coated with large V_3O_7 nanobelts and thin CNTs. The rGO-VCNT composite with 40 wt% rGO exhibited a maximum C_{sp} of 685 F g^{-1} at a current density of 0.5 A g^{-1}, which decreased to ~375 F g^{-1} at a high current density of 10 A g^{-1}. The high porosity of rGO and improved conductivity because of well-distributed CNTs resulted in an excellent rate capability. With a primarily carbon-based composition and strong bonds between V_2O_5 and CNTs, the rGO-VCNT (40 wt% rGO) electrode retained 99.7% of its initial C_{sp} after 10,000 cycles at a high scan rate of 100 mV s^{-1}. The maximum energy density of the symmetric supercapacitor was 34.3 Wh kg^{-1} at a power density of 150 W kg^{-1}, which decreased to 18.8 Wh kg^{-1} at a power density of 3000 W kg^{-1}. Mtz-Enriquez et al. reported an improved discharge time of a VCNT electrode by functionalizing the CNTs to promote V_2O_5 defects [93]. The CNTs were first deposited on a flexible graphene electrode and activated with strong acids. A V_2O_5 slurry was then applied to the CNT-coated graphene electrode and hot-pressed at 0.1 ton for physical binding. The resulting composite was comprised of rectangular V_2O_5 orthorhombic nanoribbons intercalated into a fibrous CNT structure. Oxygen vacancies formed in the V_2O_5 crystal structure due to the reduction of V^{5+} to V^{4+}, which acted as redox centers for delayed current discharge. The functionalization of CNTs with carboxylic groups also created oxygen vacancies in the carbon lattice, promoting the formation of additional V_2O_5 defects.

The CNTs also provided a secondary layer for ion storage and a large surface area for V_2O_5 contact, resulting in a high capacity and rate capability. The asymmetric supercapacitor with a graphene/VCNT anode had an energy density of 369.6 Wh kg^{-1}.

MWCNTs can also be functionalized to achieve an increase in conductivity and homogeneous V_2O_5 formation. Saravanakumar et al. functionalized MWCNTs with hydroxyl, carboxyl, and keto-carbonyl groups using concentrated H_2SO_4 and HNO_3 [94]. A mixture of functionalized MWCNTs and V_2O_5 crystals was aged for three days at room temperature to yield a V_2O_5/MWCNT (VMWCNT) composite. The orthorhombic V_2O_5 crystals formed the cores surrounded by MWCNTs, resulting in a highly porous network. Even with a relatively low carbon content of 8.73 wt%, the surface area was large (14.4 m^2 g^{-1}) because of the mesoporous web-like architecture of the MWCNTs. The VMWCNT electrode exhibited a maximum C_{sp} of 410 F g^{-1} at a current density of 0.5 A g^{-1}, which decreased to 280 F g^{-1} at a current density of 10 A g^{-1}. The high rate capability was because of the porous structure that allowed the fast intercalation/de-intercalation of ions and high conductivity of the functionalized CNT web. The functionalized CNTs improved the cyclability of the VMWCNT electrode, as indicated by 86% C_{sp} retention after 600 cycles at a high current density of 10 A g^{-1}. The symmetric supercapacitor with functionalized VMWCNT electrodes exhibited an energy density of 8.9 Wh kg^{-1} at a power density of 121 W kg^{-1}. Pandit et al. functionalized MWCNTs with carboxyl groups using H_2O_2 [95]. A stainless-steel current collector was first dip coated with the MWCNTs, and the resulting MWCNT/stainless-steel electrode was dip coated with a solution of $VOSO_4$ and NaOH. After repeated dipping and drying, the resulting VMWCNT/stainless-steel electrode had a layered structure of orthorhombic V_2O_5 flakes intercalated in a web of long MWCNTs. A C_{sp} of 629 F g^{-1} was observed at a current density of 2 A g^{-1}, which decreased to ~320 F g^{-1} at a current density of 8 A g^{-1}. The C_{sp} of the composite electrode was high because the porous structure formed by the web-like MWCNTs allowed large volumes of counterion intercalation/de-intercalation deep in the V_2O_5 crystals. The VMWCNT electrode retained 93% of its C_{sp} after 4000 cycles at a high scan rate of 100 mV s^{-1}, showing good reversibility and stability. A symmetric supercapacitor with VMWCNT electrodes yielded an energy density of 72 Wh kg^{-1} at a power density of 2300 W kg^{-1} that decreased to 18.66 Wh kg^{-1} at a power density of 8400 W kg^{-1} and current density of 4 A g^{-1}.

Different synthesis strategies, including hydro/solvothermal and deposition methods, can result in VCNT composites with different nanostructures. The hydrothermal method is a facile technique that involves the nucleation of V_2O_5 crystals from vanadium precursors on CNTs at high temperatures. Deposition techniques such as CVD allow the direct layering of V_2O_5 on CNTs with a controllable thickness. Functionalizing the CNTs with hydroxyl and carbonyl groups before synthesis with V_2O_5 can improve the overall conductivity, porosity, and stability of the hybrid material.

3.2. Effects of Composition

The ratio of V_2O_5 to CNTs affects the electrochemical performance of VCNT electrodes via changes in their morphologies, conductivities, porosities, and pseudocapacitive potentials. Guo et al. reported increases in the conductivity and rate capability with high CNT content [96]. The $V_2O_5 \cdot n H_2O$ aerogel and CNTs were dispersed in DI water, vacuum filtered with a cellulose membrane, and dried at 60 °C. The film was comprised of densely packed V_2O_5 nanosheets with homogeneously intercalated CNTs between the V_2O_5 layers, preventing V_2O_5 self-stacking. An increase in the CNT content increased the thickness of the VCNT film by increasing the interstitial space between the V_2O_5 sheets. The increased thickness prevented deep ion infiltration into the inner V_2O_5 layers near the center of the electrode. However, an increase in the CNT content increased the conductivity of the overall electrode by introducing more interlayer CNT connections, as indicated by the low square resistance of 128 Ω sq^{-1} for VCNT-10 (10 wt% CNT). VCNT-10 exhibited the highest C_{sp} of 207.7 F g^{-1} (521 F cm^{-3}) at a current density of 0.5 A g^{-1}. An increase in the CNT content increased the rate capability, with VCNT-15 (15 wt% CNT) exhibiting the

highest C_{sp} retention of 49.5% compared to the 42% retention of the VCNT-10 electrode at a high current density of 20 A g^{-1}. The flexible symmetric supercapacitor exhibited good performance in both bent and unbent states with a high energy density of 7300 Wh kg^{-1} at a power density of 42.6 W kg^{-1}. Yilmaz et al. reported similar improvements with fewer V_2O_5 nanosheets intercalated with CNT [97]. V_2O_5 gel was rigorously mixed in solutions with different amounts of CNTs, yielding free-standing electrodes consisting of V_2O_5 nanosheets with an orthorhombic crystal structure. The CNTs were homogeneously intercalated between the V_2O_5 nanosheets. An increase in the V_2O_5 content decreased the porosity of the V_2O_5 nanosheets, decreasing the overall surface area of the VCNT composite. The composite gel was printed on a 1 cm $\times$ 1 cm ITO glass plate and dried before use as an electrode. V_1CNT_2 (1:2 ratio of V_2O_5 to CNT) yielded the highest C_{sp} of 116 F g^{-1} at a current density of 0.1 A g^{-1}. An increase in the V_2O_5 loading to 1:1 ratio (V_1CNT_1) resulted in a lower C_{sp} value of 32 F g^{-1} at a current density of 0.1 A g^{-1} because of a decrease in the number of active sites on V_2O_5 nanosheets. Further addition of V_2O_5 decreased the C_{sp} due to V_2O_5 agglomeration, which decreased surface ion adsorption. Because of the highly conductive CNT linkages, the carbon-dominant V_1CNT_2 electrode exhibited a good cycling capability, with 91.2% capacitance retention after 5000 cycles at a current density of 5 A g^{-1}. A symmetric supercapacitor with V_1CNT_2 electrode yielded a volumetric energy density of 0.67 mWh cm^{-3} at a power density of 0.27 W cm^{-3}. Wu et al. fabricated a thin-film electrode with varying V_2O_5 content using a sol-gel method [98]. V_2O_5 nanobelts, CNTs, ethanol, terpilneol, and ethyl cellulose were mixed at 80 °C to yield a gel that was then doctor bladed onto a ceramic plate and annealed at 350 °C in air. The thin film was peeled off the ceramic to yield a free-standing VCNT thin film. The V_2O_5 nanobelts were highly uniform with an orthorhombic crystal phase, resulting in uniformly thick (20–100 nm) and long (>100 nm) nanobelts. A conductive current collector was added by compressing the thin-film electrode between Ti foils at 4000 psi. The VCNT-75 (75 wt% V_2O_5 composition) thin-film exhibited the highest C_{sp} of 216 F g^{-1} at a scan rate of 5 mV s^{-1}, which was five times greater than that of the bare CNTs. VCNT-75 also exhibited the highest volumetric capacitance of 540 F cm^{-3} at a scan rate of 5 mV s^{-1}, which decreased by 79% at a scan rate of 100 mV s^{-1}. The poor rate capability was due to an inefficient electron transfer caused by the low carbon composition. VCNT-61 (60.5 wt% V_2O_5) exhibited the best balance between maximum capacitance and electrode stability with a C_{sp} of 192 F g^{-1} at a scan rate of 5 mV s^{-1} and a 64% C_{sp} retention at a scan rate of 100 mV s^{-1}. Moreover, the higher CNT content increased the electron conduction, resulting in 79.8% C_{sp} retention after 5000 cycles at a scan rate of 50 mV s^{-1}. A symmetric supercapacitor with VCNT-61 electrodes yielded a maximum volumetric energy density of 41 Wh L^{-1} at a volumetric power density of ~400 W L^{-1}, which decreased to 29.1 Wh L^{-1} at a volumetric power density of 6500 W L^{-1}. A balance between conductive CNTs and energy-dense V_2O_5 is necessary for achieving the maximum electrochemical performance.

The CNT to V_2O_5 ratio changes the extent of the EDL and pseudocapacitive characteristics of the hybrid material. Perera et al. found that altering the V_2O_5 to CNT ratio can also affect the physical properties of the composite thin film [99]. A free-standing VCNT electrode was fabricated by filtering a suspension of CNTs and V_2O_5 through nylon filter paper. The VCNT-covered filter papers were dried, yielding a highly flexible thin-film supercapacitor electrode. The hybrid material was comprised of long V_2O_5 nanowires that formed a web-like structure. Short and curly CNTs were uniformly intercalated into the V_2O_5 web. Increasing V_2O_5 content decreased the porosity of the composite while increasing the CNT content increased the brittleness of the thin-film electrode. A 1:1 ratio of V_2O_5 and CNTs (V_1CNT_1) exhibited the greatest structural integrity and optimal electrochemical performance with a C_{sp} of 57.3 F g^{-1} at a current density of 0.5 A g^{-1}. The V_1CNT_1 electrode exhibited good rate capability with a C_{sp} of 42.9 F g^{-1} at a current density of 10 A g^{-1}. A coin-cell type supercapacitor with a V_1CNT_1 anode exhibited an energy density of 46.3 Wh kg^{-1} at a power density of 5260 W kg^{-1}. In comparison, the VCNTs with a 1:5 ratio of V_2O_5 to CNTs had a lower energy density of 6 Wh kg^{-1} because of the decreased

pseudocapacitive energy storage capacity. A good balance of V_2O_5 content for maximum pseudocapacitive capacity and increased CNT content for improved porosity is essential for optimized VCNT electrode performance. Such flexible, high-performance electrodes allow the development of more powerful portable and bendable technologies. Sathiya et al. reported different contributions of intercalative and capacitive charge capacities by varying the V_2O_5 content [100]. VTIP was dispersed in a suspension of pre-functionalized CNTs and stirred for one day to allow slow hydrolysis. The resulting VCNT composite gel was aged for a week, washed with acetone, dried at room temperature, and further dried at 200 °C. Long CNTs were uniformly coated with a layer of V_2O_5 crystals, resulting in a web-like structure of long V_2O_5/CNT core/shell nanotubes. Pristine CNTs relied purely on nonfaradic mechanisms for charge storage, whereas pure V_2O_5 mainly used faradic ion intercalation for charge storage. An increase in the V_2O_5 content from 0 to 25 wt% increased both faradic and nonfaradic contributions owing to the synergistic effect between the CNTs and V_2O_5. However, further increase in the V_2O_5 content decreased the faradic contribution due to increased V_2O_5 coating thickness. With a V_2O_5 loading of 25 wt%, 67% of the total stored charge was from pseudocapacitive redox reactions and surface ion adsorption. The maximum specific capacity was 850 mAh g^{-1}, which was more than twice the capacity of purely pseudocapacitive pristine V_2O_5.

Because essential factors, including conductivity, porosity, and the charge storage method, are dependent on the ratio of V_2O_5 to CNT, it is important to optimize each type of VCNT composite. In general, a higher CNT content increases the EDL contribution, conductivity, and rate capability. In contrast, a large V_2O_5 content results in a higher faradic contribution, energy storage potential, and flexibility.

3.3. Effects of Physical Treatment

Heat treatment is often used as the final step in VCNT synthesis because annealing the composite material improves the crystallinity and morphology of the composite. Sun et al. found an increased conversion of amorphous vanadium oxide to V_2O_5 after heat treatment [101]. Vertically aligned CNTs were deposited on a Si substrate via CVD and reacted with vanadium(III) acetylacetonate. Upon annealing at 350 °C in air, V_2O_5 microspheres were uniformly grown on the CNT surface. Annealing the composite converted the vanadium precursor to V_2O_5 and improved the crystallinity of the vanadium oxide precursor. Even after high-temperature annealing, the composite contained mixed valence states of vanadium oxide, which enhanced the ion diffusion. The C_{sp} of the VCNT composite was 284 F g^{-1} at a current density of 2 A g^{-1}, which decreased by ~50% at a high current density of 15 A g^{-1}. The direct growth of V_2O_5 on the CNTs improved the surface contact, thereby decreasing the charge transfer resistance to 1.2 Ω and resulting in good rate performance. Moreover, interstitial spacing between the vertically aligned CNTs provided a spacious environment that decreased the internal strain during charge/discharge, resulting in a high C_{sp} retention of 89.3% after 2500 cycles at a high current density of 10 A g^{-1}. An asymmetric supercapacitor with the VCNT electrode had an energy density of 32.3 Wh kg^{-1} at a power density of 118 W kg^{-1}. Similarly, Wang et al. reported increased V_2O_5 formation after calcination [102]. A solution of NH_4VO_3, CNTs, super AC (SAC), and DI water was reacted in an autoclave at 180 °C for one day and subsequently calcined in a muffle furnace at 250 °C for 6 h in air. The resulting VCNT material had orthorhombic V_2O_5 sheets interspaced with thick CNTs and SAC bundles. The addition of CNTs increased the BET surface area from 14 to 19 m^2 g^{-1}, and the addition of both CNTs and SAC further increased the surface area to 78 m^2 g^{-1} because of the increased mesopore volume. The VCNT electrode without SAC outperformed pristine V_2O_5 with a C_{sp} of 231.8 F g^{-1} at a high current density of 10 A g^{-1}. A high C_{sp} was observed even at a high current density because of the improved conductivity provided by the intercalated CNTs and short ion diffusion pathways to the crystalline V_2O_5 sheets. Moreover, the VCNT electrode with SAC yielded a maximum C_{sp} of 357.5 F g^{-1} because of the increased surface area that provided more activation sites. Shakir et al. synthesized a VMWCNT material through a

heat-induced reaction and further annealed the composite at 350 °C for 2 h under ambient conditions [103]. The resulting VMWCNT thin film had layers of highly orthorhombic V_2O_5 crystals surrounded by long and curly MWCNTs. VMWCNTs that were 3 nm thick exhibited the highest C_{sp} of 510 F g^{-1} at a scan rate of 1 mV s^{-1} because the thickness maximized the surface area-to-volume ratio of V_2O_5. The C_{sp} of the composite was significantly higher than that of bare MWCNTs at 80 F g^{-1} because of the pseudocapacitive reactions enabled by the V_2O_5 crystals. The VMWCNT electrode exhibited good stability with 96% of its initial C_{sp} retained after 5000 cycles at a high scan rate of 20 mV s^{-1} because of the improved conductivity of the MWCNTs and structural stability of the web-like nanostructure. The energy density of the electrode was 16 Wh kg^{-1} at a power density of 800 W kg^{-1}. Physical treatment is a key component of VCNT synthesis because it promotes the conversion of amorphous vanadium oxides to a more crystalline V_2O_5.

4. V_2O_5/CNFs

CNFs have attracted significant attention as a substrate material for V_2O_5 growth because of their ease of synthesis, pore size controllability, and high conductivity [104]. Moreover, their stable 3D structures allow them to be used as free-standing electrodes for decreased internal resistance, high porosity, and flexible electrode applications [105]. V_2O_5/CNF (VCNF) composites often comprise either a CNF/V_2O_5 core/shell structure, V_2O_5 crystal growth on long CNFs, or V_2O_5 crystals intercalated in the CNF pores. The effects of the synthesis method, V_2O_5 content, and physical treatment on the electrochemical performances of the VCNF composite electrodes are reviewed. The morphology and electrochemical performances of V_2O_5/CNF electrodes for supercapacitor applications reported in the literature are summarized in Table 3.

4.1. Effects of Synthesis Method

Electrodeposition is a common technique used to form a V_2O_5 coating on long carbon fibers, resulting in a CNF/V_2O_5 core/shell structure. Song et al. used electrodeposition to coat the nanofibers of exfoliated carbon cloth (CC) with V_2O_5 [106]. The architecture of the fibrous structure was preserved, and two additional layers, an exfoliated carbon middle layer and a V_2O_5 outer layer, were added to the preexisting nanofibers. Due to a lack of heat or catalyst during electrodeposition, only half of the initial V_2O_5 precursor was oxidized, resulting in amorphous, mixed-valence V_2O_5. The areal capacitance of the device was 106 F cm^{-2} at a current density of 2 mA cm^{-2}, which decreased by 24% at a current density of 20 mA cm^{-2}. The good rate capability was attributed to the conductive carbon skeleton and improved electron mobility through the V-O-C bonds in the exfoliated carbon middle layer. Unlike most electrodes that degrade with repeated cycling, a 40% increase in the C_{sp} of the exfoliated VCNF electrode was observed after 10,000 cycles at a current density of 60 mA cm^{-2} because of the activation of the material via ion intercalation/de-intercalation. Repeated cycling introduced more intercalated water molecules, which expanded the interlayer distance for additional active sites. Water also shuttled the electrolyte ions during intercalation/de-intercalation. A similar V^{4+} to V^{5+} ratio decreased the dissolution of the V_2O_5 crystals during charge/discharge for improved stability.

Table 3. V_2O_5 morphology and electrochemical performances of V_2O_5/carbon nanofiber composite electrodes for supercapacitor applications.

Morphology	Maximum C_{sp} (F g^{-1})	Cycling C_{sp} Retention (%)	Cycle Number	Energy Density (Wh kg^{-1})	Power Density (W kg^{-1})
Nanorods	535.3	91.1	5000	38.7	900
CNF Coating	-	-	-	101	27,370
Nanosheets	-	89.3	10,000	40.2	800
CNF Coating	227	89	2000	63.6	400
CNF Coating	-	94 *	10,000 *	17.7	2728
Nanospheres	475.5	89.7 *	6000 *	-	-
Nanohairs	460.8	92 *	10,000 *	48.32	490

* Cycling performance was determined using a two-electrode configuration.

Crystallization can be used to coat CNFs with V_2O_5. Zhou et al. synthesized a high-performance V_2O_5/polyindole/ACC (VPIAC) composite electrode via crystallization [107]. Activated carbon cloth (ACC) was synthesized via CC activation with HNO_3, H_2SO_4, and $KMnO_4$, followed by heat-induced reduction in N_2/H_2 (95%/5%) atmosphere at 1000 °C. Sodium metavanadate was dripped onto the ACC and crystallized at 400 °C. Subsequently, a solution of H_2O_2, indole, and DI water was dripped onto V_2O_5/ACC to promote V^{4+} oxidation to V^{5+}. The resulting composite exhibited a bamboo-like structure with V_2O_5 and polyindole anchored to the surface of the long nanofibers. The electrochemical performance of the composite electrode was determined using a three-electrode configuration with a Pt counter electrode, Ag/AgCl reference electrode, and 5 M $LiNO_3$ electrolyte. The VPIAC hybrid material exhibited a high C_{sp} of 535.3 F g^{-1} at a current density of 1 A g^{-1} because of the increased conductivity of the polyindole. The VPIAC electrode had a low series resistance and charge transfer resistance of 1.1 and 7.6 Ω, respectively. The hybrid material exhibited excellent 91.1% C_{sp} retention after 5000 cycles at a high current density of 10 A g^{-1} because the polyindole decreased the dissolution of V_2O_5 during charge/discharge and increased adhesion between the CNFs and V_2O_5. The energy density of an asymmetric supercapacitor with the VPIAC electrode was 38.7 Wh kg^{-1} at a power density of 900 W kg^{-1}, which decreased to 32.6 Wh kg^{-1} at a power density of 18,000 W kg^{-1}.

The sol-dipping method can also allow the uniform coating of CNFs with a V_2O_5 shell. Azadian et al. employed a sol-dipping method involving the repeated dipping and drying of polyacrylonitrile-based carbon paper into a V_2O_5 sol [108]. The dip–dry process was performed multiple times to promote the growth of a thick layer of V_2O_5 crystals on the carbon paper nanofibers. The V_2O_5 grown on the CNFs exhibited a high C_{sp} of 800 F g^{-1}. Because of the porous architecture of the carbon fibers, the intercalation/de-intercalation was highly reversible, yielding a high Coulombic efficiency of 92%. The energy density of the electrode was 101 Wh kg^{-1} at a power density of 27 370 W kg^{-1}.

In addition to the formation of a CNF/V_2O_5 core/shell nanostructure, small V_2O_5 nanoparticles can be intercalated within the porous CNFs. Zhou et al. fabricated a CC-based electrode with V_2O_5 nanosheets embedded within the CNF webs [109]. CC/graphene foam/$CoMoS_4$ was mixed with a V_2O_5 supernatant for 12 h. The $CoMoS_4$ bound to CC/graphene resulted in the uniform coating of thin $CoMoS_4$ nanowires on the smooth CNFs, and the nanowires hosted the V_2O_5 nanosheets. The cyclic voltammetry (CV) curves of the hybrid material exhibited a distinct peak, indicating a large pseudocapacitive contribution. The CV curves retained their shape upon increasing scan rates from 5 to 50 mV s^{-1}, indicating good rate capability owing to the conductive carbon matrix (Figure 6a). The composite behaved more like a battery instead of a capacitor, based on the large IR drop shown in the galvanostatic charge–discharge (GCD) plot in Figure 6b. The specific capacity of the electrode was 158.6 mAh g^{-1} at a current density of 1 A g^{-1} (Figure 6c).

Vanadium promoted faradic redox reactions, which increased the charge storage potential of the electrode. The addition of graphene to the carbon fibers enhanced the charge transfer from V_2O_5 to the current collector and functioned as a buffer to prevent physical deformation during intercalation/de-intercalation. Thus, the hybrid material was highly cyclable with a >90% C_{sp} retention after 5000 cycles (Figure 6d). An asymmetric supercapacitor with a V_2O_5/$CoMoS_4$/CC/graphene positive electrode exhibited an energy density of 40.2 Wh kg^{-1} at a power density of 800 W kg^{-1}.

Unlike other synthesis strategies for growing V_2O_5 on a carbon nanofiber substrate, the electrospinning technique can directly produce VCNF composite materials [110]. The placement of a solution of a carbonaceous material such as polyacrylonitrile (PAN) and V_2O_5 in an electrospinning apparatus resulted in a flexible nanofiber composite material with controllable porosity and composition [111]. Kim et al. electrospun VCNF fibers using a dispersion of PAN and different amounts of V_2O_5 in a DMF solution [112]. The resulting nanofibers were heat treated at 800 °C under a nitrogen atmosphere for further oxidation and stabilization. The resulting nanofiber structure was primarily composed of

carbon with small, amorphous V_2O_5 agglomerations anchored on the CNF surface. The size of the agglomerations increased from 20 to 80 nm with an increase in the V_2O_5 content. Increasing the V_2O_5 content also increased the surface area of the electrode by introducing more pores into the nanofiber structure. The BET surface area of VCNF-20 (20 wt% V_2O_5) was 595.21 m^2 g^{-1} compared to 510.45 m^2 g^{-1} for VCNF-5 (5 wt% V_2O_5). In a symmetric electrode setup, the VCNF-20 electrode exhibited a C_{sp} of 150.0 F g^{-1} at a current density of 1 mA cm^{-2}, which was three times greater than that of the bare CNF because of the faradic contributions from the V_2O_5 crystals.
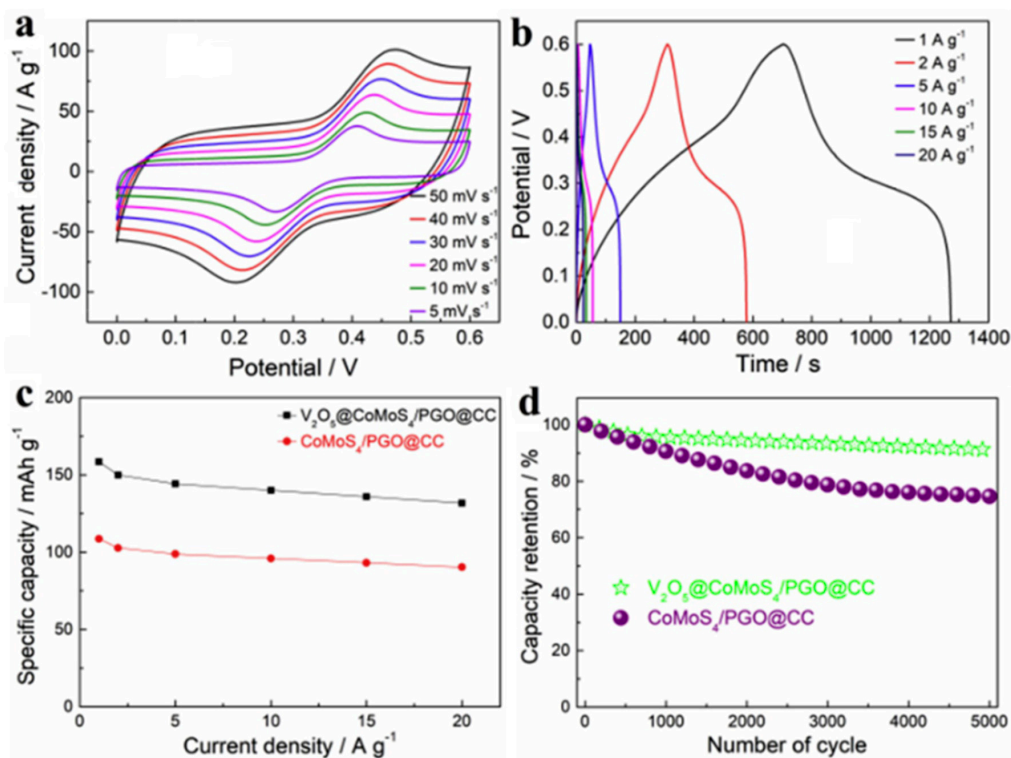
Figure 6. (**a**) CV and (**b**) GCD curves of V_2O_5/$CoMoS_4$/CC/graphene at different scan rates and current densities, respectively. (**c**) C_{sp} values of V_2O_5/$CoMoS_4$/CC/graphene and $CoMoS_4$/CC/graphene at different current densities and (**d**) cycling performances of V_2O_5/$CoMoS_4$/CC/graphene and $CoMoS_4$/CC/graphene. Reprinted with permission from Ref. [109]. Copyright 2020 Elsevier.

Various synthesis methods are available for the fabrication of VCNF hybrid materials. Strategies that involve the coating of nanofibers on a CC substrate, such as electrodeposition, sol dipping, and crystallization, utilize the porous architecture and high conductivity of CNFs for improved electrochemical performance. Alternatively, V_2O_5 nanocrystals can be intercalated into the CNFs for similar benefits. Electrospinning can be used to synthesize a VCNF material without any dependence on the CNF substrate. Instead, V_2O_5 and the carbon precursor can be electrospun into a fibrous product, allowing easily controllable composition and porosity.

4.2. Effects of Composition

The ratio between CNF and V_2O_5 plays a vital role in determining the electrochemical properties of a VCNF composite by altering its conductivity, porosity, and morphology. Kim et al. electrospun a solution with varying V_2O_5 loading and PA [113]. The mixture was subsequently heat treated and steamed under a nitrogen atmosphere at 800 °C for 1 h for carbon activation. The activated VCNF material had a fibrous structure with V_2O_5 agglomerations of 15 to 60 nm in diameter. The size of the agglomerations increased with increasing V_2O_5 loading owing to a change in the viscosity and conductivity of the

electrospun solution. The activation of the nanofibers increased the diameter from 108 to 200 nm. A lower V_2O_5 content increased the surface area of the composite with a maximum BET surface area of 1113.5 $m^2\,g^{-1}$ for activated VCNF-5 (5 wt% V_2O_5) because more carbon was accessible for activation by the steam. Activated VCNF-5 had the greatest C_{sp} (73.85 $F\,g^{-1}$) at a current density of 1 $mA\,cm^{-2}$, which decreased slightly to 58.02 $F\,g^{-1}$ at a large current density of 20 $mA\,cm^{-1}$ because of its low charge transfer resistance of 1.20 Ω. The symmetric supercapacitor with activated VCNF-5 electrodes had an energy density of 68.84 $Wh\,kg^{-1}$ at a power density of 20,000 $W\,kg^{-1}$.

The composition of V_2O_5 and CNF can be altered by changing the duration of V_2O_5 exposure to the CNF substrate. Choudhury et al. submerged CNF paper in a solution of V_2O_5 and H_2O_2 for five and seven days [114]. The resulting free-standing paper electrode was dried at 100 °C for one day in an oven. Increased exposure to V_2O_5 resulted in more V_2O_5 crystallization on the CNFs. VCNF-5 (five days) had a V_2O_5 layer thickness of ~8 nm, whereas VCNF-7 (seven days) had a thickness of ~17 nm. Although both VCNF variants were limited by the incomplete oxidation of V_2O_5, VCNF-5 exhibited higher crystallinity and decreased water intercalation because of the shorter exposure to the V_2O_5 solution. VCNF-5 also had a larger BET surface area of 573.65 $m^2\,g^{-1}$ compared to the surface area of 442.16 $m^2\,g^{-1}$ for VCNF-7 because each nanofiber in VCNF-5 was thinner, resulting in larger pore sizes. VCNF-5 exhibited larger EDL characteristics than VCNF-7 because VCNF-5 had a higher amount of accessible carbon content. VCNF-5 yielded a C_{sp} of 227 $F\,g^{-1}$ at a current density of 1 $A\,g^{-1}$. The C_{sp} decreased slightly to 154 $F\,g^{-1}$ at a current density of 10 $A\,g^{-1}$ because of its low 5.49 Ω charge transfer resistance. The VCNF-5 electrode had a maximum energy density of 63.6 $Wh\,kg^{-1}$ at a power density of ~400 $W\,kg^{-1}$, which decreased to 18.8 $Wh\,kg^{-1}$ at a power density of 4555 $W\,kg^{-1}$. Velayutham et al. examined the importance of electrodeposition duration on the composition of binderless VCNF electrodes [115]. Rope-like V_2O_5 with a pure orthorhombic crystal phase was evenly deposited onto the carbon fibers, resulting in V_2O_5 surface extrusions. The wrinkled surface from the V_2O_5 crystal growths resulted in a greater surface area for faradic redox reactions. Increasing the deposition time beyond 40 min resulted in a smoother surface because of the increased V_2O_5 growth, leading to a smaller surface area. VCNF-40 (40 min deposition) exhibited the highest areal capacitance of 394 $mF\,cm^{-2}$ at a current density of 1 $mA\,cm^{-2}$. A 40 min deposition time had a large V_2O_5 composition for higher energy storage potential while creating a rough CNF coating for more surface redox reactions. At higher scan rates, VCNF-30 performed better than VCNF-40 with an areal capacitance of 143 $mF\,cm^{-2}$ at a current density of 15 $mA\,cm^{-2}$ because the higher carbon composition improved the electron mobility. An asymmetric supercapacitor with a VCNF-30 positive electrode yielded an energy density of 17.7 $Wh\,kg^{-1}$ at a power density of 2728 $W\,kg^{-1}$.

The composition of VCNF composites can be altered by controlling the initial loading of V_2O_5 during synthesis or exposing a CNF substrate to V_2O_5 for different durations of time. Optimizing the composition of the VCNF material is essential for maximizing the faradic energy storage potential while maintaining high porosity and conductivity for the hybrid material.

4.3. Effects of Physical Treatment

The heat treatment of the VCNF composites improves their stability and increases V_2O_5 oxidation for better electrochemical performance. Chen et al. formed arrays of thin V_2O_5 nanosheets on a CC template via a hydrothermal synthesis route and subsequently annealed the composite at different temperatures in an H_2/argon atmosphere [116]. An increase in the annealing temperatures created more defects in the V_2O_5 crystal structure, and the non-uniform crystal structure resulted in high ion diffusion and fast redox reactions. The VCNF material contained amorphous V_2O_5 nanosheets with more metallic than semiconductor characteristics due to the oxygen defects. Figure 7 summarizes the effects of annealing on the formation of defects for enhanced electrochemical performance. The VCNF annealed at the highest temperature of 500 °C yielded the highest areal capacitance

of 554 mF cm^{-2} at a current density of 0.63 A g^{-1}. An asymmetric supercapacitor with the VCNF electrode exhibited an energy density of 161.8 μWh cm^{-2} at a power density of 500 μW cm^{-2}. You et al. found that annealing a VCNF composite at different temperatures affected the formation of V$_2$O$_5$ agglomeration [117]. A VCNF composite was synthesized via a hydrothermal process and subsequently annealed at 500 °C in a nitrogen atmosphere for different durations. V$_2$O$_5$ had a partial orthorhombic crystal structure owing to the incomplete oxidation of V$_2$O$_5$ during the hydrothermal process. Long annealing durations increased the size of the V$_2$O$_5$ agglomeration on the CNF surface. VCNF-24 (24 h annealing) contained a uniform distribution of V$_2$O$_5$ nanospheres coating the CNFs. However, an increase in the annealing time to 48 h resulted in large agglomerations of V$_2$O$_5$, decreasing the number of V$_2$O$_5$ active sites for surface redox reactions. With a homogeneous distribution of V$_2$O$_5$ crystals on the CNFs, VCNT-24 outperformed the other electrodes. VCNT-24 yielded a high C$_{sp}$ of 475.5 F g^{-1} at a current density of 1 A g^{-1}, more than three times that of pristine V$_2$O$_5$. With many V$_2$O$_5$ nanospheres, most of the capacitance was attributed to ion diffusion instead of surface capacitance. A flexible asymmetric supercapacitor with a VCNT-24 positive electrode exhibited a volumetric energy density of 0.928 mWh cm^{-3} at a power density of 17.5 mW cm^{-3}.

Annealing the composite material also allowed the formation of doped VCNF composites. Guo et al. doped a VCNF composite with additional carbon to form carbon/V$_2$O$_5$ core/shell nanowires on a CNF substrate [118]. First, the VCNF electrode was fabricated via a hydrothermal technique. The VCNF was then dipped in a glucose solution and heat-treated at 500 °C under a nitrogen atmosphere, resulting in C-doped VCNF. The overall nanofibrous macrostructure of CC was preserved after heat treatment. The long CNFs were uniformly coated with thin strands of long V$_2$O$_5$ nanowires. The annealed glucose coated the thin V$_2$O$_5$ strands with an outer layer of carbon. The C-doped VCNF electrode exhibited an areal capacitance of 128.5 mF cm^{-2} at a scan rate of 10 mV s^{-1}, which decreased by 60% at a scan rate of 400 mV s^{-1}. The good rate capability was because of the additional carbon coating that increased the conductivity. The areal capacitance was 164.2 F cm^{-2} at a current density of 0.5 A cm^{-2}, with major contributions from both faradic and EDL characteristics. The charge transfer resistance (3.8 Ω) was low because of the conductive contact between the CNFs on the CC and the outer carbon layer on the V$_2$O$_5$ nanowires. The carbon coating also reduced vanadium dissolution, resulting in high cyclic stability, as indicated by a high 94.4% C$_{sp}$ retention after 10,000 cycles at a high scan rate of 100 mV s^{-1}, which was significantly higher than that of pure V$_2$O$_5$ (13.3%). Sun et al. doped CNFs with nitrogen by first preparing a solution of CNF, pyrrole monomer, and ammonium persulfate and subsequently heating the mixture to 900 °C under argon atmosphere for 2 h, yielding an N-doped CNF (N-CNF) composite [119]. A V$_2$O$_5$ sol was added dropwise into the N-CNF material to yield a sol-gel that was subsequently cured for two days in an oven at 50 °C. The resulting aerogel was freeze dried and annealed at 350 °C in air, yielding a free-standing N-VCNF electrode. The N-CNFs were coated with a 20-nm-thick layer of V$_2$O$_5$. The V$_2$O$_5$ layer constituted a pure orthorhombic crystal phase, suggesting the complete oxidation of V^{4+} to V^{5+} due to the annealing procedure. The addition of the V$_2$O$_5$ layer to the N-CNFs decreased the BET surface area to 334.2 m^2 g^{-1}. The C$_{sp}$ of N-VCNF was 595.1 F g^{-1} at a current density of 0.5 A g^{-1}, which was almost twice that of the non-doped VCNF. The nitrogen substitutions in the CNF lattice functioned as nucleation sites for additional V$_2$O$_5$ crystal growth, allowing a more uniform formation of the core/shell microstructure. The homogeneous V$_2$O$_5$ coating decreased the charge transfer resistance to 1.04 Ω. The N-VCNF electrode exhibited good reversibility with almost no change in C$_{sp}$ after 10,000 cycles at a current density of 0.5 A g^{-1} and only a 3% decrease after 12,000 cycles because of the stable core/shell nanostructure. The symmetrical supercapacitor with N-VCNF electrodes had a maximum energy density of 82.65 Wh kg^{-1} at a power density of 250 W kg^{-1} which decreased to 26.83 Wh kg^{-1} at a power density of 5000 W kg^{-1}.
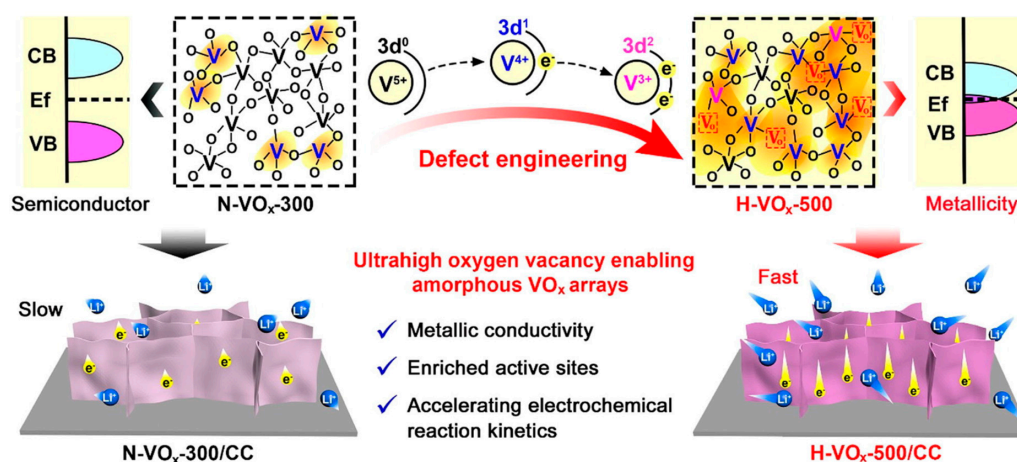
Figure 7. Schematic of the regulation of the V 3d band edge with high electrical conductivity by defect engineering and electrochemical advantages of the as-formed metallic amorphous VO_x nanosheet arrays. Reprinted with permission from Ref. [116]. Copyright 2021 Elsevier.

In addition to the heat treatment, other physical treatments can alter the morphology of the VCNF electrodes. Parmar et al. further modified the V_2O_5 crystals grown on carbon fiber surfaces using lasers to dehydrate amorphous V_2O_5 crystals [120]. A VCNF material with intercalated water molecules was synthesized via electrodeposition. Pristine V_2O_5 had an interstitial spacing of ~4.4 Å with an alternating VO_5–VO_5 pyramid structure, whereas hydrated V_2O_5 had a spacing that was two to three times greater than that of the atomic pyramids facing the same direction. De-intercalating water from the crystal structure of V_2O_5 decreased the interlayer gap to ~4 Å, reverting the atomic structure to the alternating pyramid form. Panigrahi et al. grew hair-like V_2O_5 crystals on AC felt but restrained one side of the AC felt to a glass slide [121]. Thus, V_2O_5 formation occurred only on the exposed side, allowing better electrical contact on the uncoated side. The acid-activated carbon felt acted as a porous template, resulting in a large BET surface area of 76.434 m^2 g^{-1} for better ion diffusion. The porous architecture of the hair-like V_2O_5 resulted in a greater pseudocapacitive contributions than EDL contributions, resulting in a high C_{sp} of 460.8 F g^{-1} at a current density of 2 A g^{-1}. The highly interconnected CNF structure increased the rate capability such that C_{sp} only decreased to 81.25% at 10 times the current density. The good electron mobility of the hybrid material was further supported by a low series resistance of 2.7 Ω and charge transfer resistance of 1.1 Ω. A symmetric supercapacitor with the VCNF electrode exhibited an energy density of 48.32 Wh kg^{-1} at a power density of 490 W kg^{-1}.

5. Other V_2O_5/Carbon Composites

Many studies have been conducted on other V_2O_5/carbon (VC) composites based on carbon moieties such as carbon quantum dots (CQDs) or bio-based carbon materials. As a stable, green, and conductive material, carbon can be added as supplementary materials to enhance the pseudocapacitive performance of V_2O_5 for supercapacitor applications [122]. These VC hybrid materials can be synthesized with carbon obtained from both inorganic and organic sources for diverse composite nanostructures. Herein, the effects of the synthesis process, V_2O_5/carbon composition, and physical treatment on the electrochemical performances of other carbon-based V_2O_5 composites are discussed. The morphology and electrochemical performances of other V_2O_5/carbon composite electrodes for supercapacitor applications reported in the literature are summarized in Table 4.

Table 4. V_2O_5 morphology and electrochemical performances of other V_2O_5/carbon composite electrodes for supercapacitor applications.

Morphology	Maximum C_{sp} (F g^{-1})	Cycling C_{sp} Retention (%)	Cycle Number	Energy Density (Wh kg^{-1})	Power Density (W kg^{-1})
Amorphous	120	89	10,000	-	-
Nanorods	300	87 *	5000 *	-	-
Nanoflowers	417	92.3	2250	47	224
Nanoflowers	-	88 *	25,000 *	33.4	670
Nanobelts	281	87	2000	-	-
Nanorods	313	81	4000	-	-
Amorphous	157.7	93 *	10,000 *	87.6	497
Nanosheets	487	84	2000	12.8	317
Nanobelts	406	13.8	100	245.7	396
Nanobelts	260	92	5000	-	-

* Cycling performance was determined using a two-electrode configuration.

5.1. Effects of Synthesis Method

The final nanostructure of the VC composite material depends significantly on the initial carbon precursor. Daubert et al. compared the morphologies of the VC electrodes synthesized using either microporous Supra 50 or mesoporous G60 carbon powders [123]. Both carbon powders were activated with concentrated acid and pasted on Ni foil with an acetylene black filler and PVDF binder. V_2O_5 was subsequently coated on the carbon-coated Ni foam using atomic layer deposition (ALD). The resulting hybrid material had a layer of amorphous V_2O_5 crystals covering the carbon surface. Additional V_2O_5 deposition cycles resulted in increasingly uneven V_2O_5 coatings. For mesoporous G60, the maximum C_{sp} was 540 F g^{-1} with 25 ALD cycles and 120 F g^{-1} for 75 ALD cycles. The high capacitance was due to the even V_2O_5 surface coating, thereby providing a large surface area for more ion adsorption. Because the micropores of Supra 50 matched the size of the atomic layer deposition precursor, the deposition process could not effectively coat Supra 50. Moreover, the coating process blocked the formation of micropores and decreased the number of active sites for faradic redox reactions. Thus, carefully selecting the carbon precursor is essential in maximizing the VC hybrid material's electrochemical performance.

Bio-based carbon sources have also been utilized for the synthesis of VC materials. Glucose is a promising carbon precursor for VC materials because it can act as an oxidizing agent at high temperatures and function as a conductive carbon additive [124]. Narayanan employed a facile hydrothermal synthesis method using V_2O_5 powder and glucose as precursors to yield VC [125]. The VC material was composed of V_2O_5 nanorods with glucose-derived carbon quantum dots (CQDs) uniformly scattered on the nanorod surface. Incomplete oxidation of V^{4+} to V^{5+} was observed due to partial reduction by glucose; however, the V_2O_5 rods still exhibited an orthorhombic crystal structure. The electrochemical performance of the VC material was tested using a three-electrode configuration with a CQD counter electrode and an Ag/AgCl reference electrode in 3 M KCl electrolyte. The C_{sp} of VC was 300 F g^{-1} at a current density of 0.5 A g^{-1}, which decreased slightly to 250 F g^{-1} at a current density of 2 A g^{-1}. The intercalated CQDs improved the conductivity of the device, as indicated by a low charge transfer resistance of 14.5 Ω. Moreover, the layered crystal structure of the V_2O_5 nanorods allowed better electron mobility via the attached CQDs. An asymmetric cell with a VC working electrode yielded a C_{sp} of 119 F g^{-1} at a current density of 1 A g^{-1}. The energy density was 60 Wh kg^{-1} at a current density of 1 A g^{-1}. The maximum power density was 4200 W kg^{-1} at a current density of 5 A g^{-1}. Balasubramanian et al. used dextran, a naturally occurring polysaccharide, as the carbon precursor [126]. Dextran was slowly added to a solution of V_2O_5 and H_2O_2 and stirred for 4 h to allow precipitation. The precipitate was subsequently annealed at 400 °C for 2 h to yield a VC hybrid material. The composite exhibited a flower-like macrostructure with urchin-like protrusions. The soft dextran decomposed and covered V_2O_5 in a sharp

urchin-like structure after annealing. The amorphous carbon layer increased the conductivity of VC and reduced V_2O_5 dissolution during charge/discharge. The flower-like architecture increased the surface area of the composite, resulting in more active sites for ion intercalation/de-intercalation, increasing the C_{sp} value to a maximum of 417 F g^{-1} at a current density of 0.5 A g^{-1}. The energy density of the VC composite was 47 Wh kg^{-1} at a power density of 224 W kg^{-1}.

The carbon sources used for VC synthesis can also be derived from once-living organisms. Ngom et al. fabricated VC electrodes from different strains of hibiscus flower: light red (LR), dark red (DR), and white (W) [127]. The flowers were dried in sunlight and crushed into powder. The powder was dissolved in DI water and filtered to remove the large organic residue. The V_2O_5 powder was added to the solution with H_2O_2 and subsequently heated in an autoclave for one day at 180 °C. The hibiscus-derived graphitic flakes were used as the template for V_2O_5 growth, resulting in the nucleation of flower-like V_2O_5 nanosheets. H_2O_2 promoted the exfoliation of the carbon flakes, resulting in a more porous structure that allowed better ion diffusion. DR-VC exhibited the largest orthorhombic crystal size, with the largest specific surface area of 3.3 m^2 g^{-1}. Due to the increased surface area and organized crystal structure, DR-VC exhibited the highest specific capacity of 99.1 mAh g^{-1}. An asymmetric supercapacitor with DR-VC and AC electrodes yielded an energy density of 33.4 Wh kg^{-1} at a power density of 670 W kg^{-1}. Mei et al. pyrolyzed bacterial cellulose to yield carbonized bacterial cellulose (CBC), which was reacted with V_2O_5 powder via a hydrothermal method [128]. The resulting composite comprised web-like carbon strands coated with thick V_2O_5 nanobelts with a width of ~70 nm and length of ~600 nm. The amorphous carbon strands formed a highly conductive web that prevented V_2O_5 aggregation. The orthorhombic crystal phase V_2O_5 supported the faradic redox reactions, and both EDL and pseudocapacitive characteristics contributed to charge storage. The C_{sp} was 198 F g^{-1} at a scan rate of 10 mV s^{-1}, which decreased to ~75 F g^{-1} at a scan rate of 200 mV s^{-1}. The CBC/V_2O_5 composite had a maximum C_{sp} of 281 F g^{-1} at a current density of 0.25 A g^{-1}, which decreased to 65 F g^{-1} at a current density of 5 A g^{-1}. The high C_{sp} at a lower current density was due to the increased pseudocapacitive contribution from V_2O_5. The CBC/V_2O_5 electrode exhibited a high cyclic stability with 97% C_{sp} retention after 1000 cycles and 87% of its initial C_{sp} after 2000 cycles at a high scan rate of 100 mV s^{-1} because of the highly conductive carbon network. The V_2O_5/CBC electrode was highly reversible because the carbon webs stabilized the V_2O_5 nanobelts.

The initial carbon precursor is vital for determining the final morphology of the VC composite. A carbon source with large pores provides a large surface area for V_2O_5 nucleation and more active sites for faradic redox reactions. Bio-derived carbon materials from various sources such as glucose, plants, and bacteria have organized carbon structures that can be carbonized and combined with V_2O_5 to improve conductivity and structural stability.

5.2. Effects of Composition

The ratio of the carbon component to V_2O_5 affects the synergetic balance between conductivity and charge capacity and can also alter the morphology of the resulting composite. Fleischmann et al. varied the ratio of V_2O_5 to carbon onion precursors for hydrothermal synthesis [129]. Figure 8 shows the SEM micrographs of V_2C_7 (2:7 V_2O_5 to carbon onion), V_3C_6 (3:6 V_2O_5 to carbon onion), and V_4C_5 (4:5 V_2O_5 to carbon onion). Fleischmann et al. also physically combined the carbon onions and V_2O_5 crystals after synthesizing each of these individually (C_5V_4-COMP).

Quasi-spherical V_2O_5 nanoflowers were grown at the nucleation sites on the carbon onions. Thus, an increase in the initial carbon content also increased the V_2O_5 growth. An increase in the carbon onion content resulted in a larger surface area for additional surface reactions. V_2C_7 (Figure 8A) was more spread out with smaller agglomerations than V_3C_6 (Figure 8B). Increasing V_2O_5 content to V_4C_5 (Figure 8C) produced larger V_2O_5 agglomerations, as indicated by the dark coloring. Physical mixing of carbon onions and

V_2O_5 resulted in large agglomerations of vanadium oxide and carbon onions (Figure 8D), which prevented the synergy between the two materials. The various VC composites were analyzed using a two-electrode configuration with a PTFE-bound AC counter electrode and a VC working electrode with $LiClO_4$ in acetonitrile electrolyte. V_3C_6 outperformed the other three composites because of well-integrated conductive carbon with a large surface area and sizable V_2O_5 growth. Zhang et al. reported an increase in conductivity with an increase in the carbon content [130]. V_2O_5 was combined with mesoporous carbon hollow spheres (MCHSs) in different ratios to form a suspension that was rigorously stirred and subsequently freeze dried to yield a macroporous VC composite. The hybrid material comprised a web-like V_2O_5 maze with sporadic MCHS nanospheres anchored to the webs. Increasing the weight percentage of MCHSs from 33% (VC-33) to 67% (VC-67) increased the number of spherical carbon agglomerations. VC-33 had sparse carbon nanospheres, whereas VC-67 formed grape-like bundles on the V_2O_5 webs. VC-50 (50 wt% MCHS) contained a uniform spread of graphitic carbon nanospheres on the V_2O_5 web. A low carbon content reduced agglomerations that allowed ion adsorption into V_2O_5. However, an increase in the carbon content increased the conductivity of the material. Thus, VC-50 with a uniform distribution of carbon nanospheres exhibited the highest C_{sp} of 313 F g^{-1} at a current density of 0.25 A g^{-1}. The macroporous web structure decreased the stress due to repeated ion insertion/de-insertion, resulting in an increase in cyclability from 43% for bare V_2O_5 to 81% for VC-50 after 4000 cycles at a current density of 5 A g^{-1}.
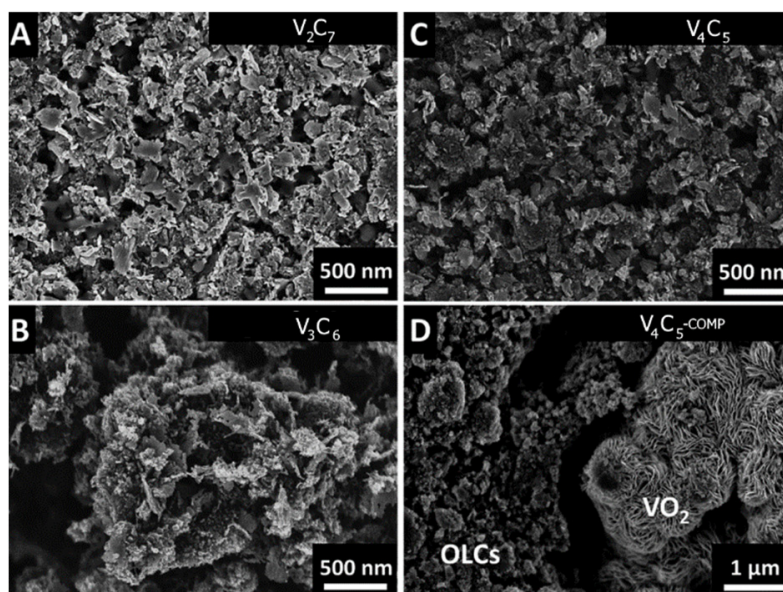

Figure 8. SEM micrographs of (**A**) V_2C_7, (**B**) V_3C_6, (**C**) V_4C_5, and (**D**) V_4C_5-COMP. Reprinted with permission from Ref. [129]. Copyright 2017 Royal Society of Chemistry.

Control of the carbon to V_2O_5 ratio can also change the porosity of the VC material, thereby altering the ion diffusion capability and number of active sites for faradic redox reactions. Zhu et al. determined the effects of V_2O_5 loading on the porosity and performance of a VC electrode [131]. The VC composite was synthesized using a liquid-phase impregnation technique, yielding a hierarchically porous VC material. The VC material had a macroporous carbon frame with V_2O_5 intercalated through the pores. At a low 17.6 wt% of V_2O_5 (VC-18), the pores in the carbon were small and tightly packed, resulting in a BET surface area of 622 m^2 g^{-1}. At a high V_2O_5 loading of 52 wt% (VC-52), the sheets were covered with large micropores with tiny gaps between the layers, resulting in a smaller BET surface area of 487 m^2 g^{-1}. The VC material with a 38.7 wt% V_2O_5 (VC-39) had the greatest BET surface area of 645 m^2 g^{-1} because of its larger pores. Thus, VC-39 yielded the highest C_{sp} of 492.1 F g^{-1} at a scan rate of 5 mV s^{-1} because of the numerous active

sites provided by the micropores and ease of ion diffusion through the high volume of macropores. The C_{sp} value decreased slightly to ~400 F g^{-1} at a scan rate of 100 mV s^{-1}, indicating good rate capability because the amorphous carbon dispersion enabled good electron mobility with low series and charge transfer resistances of 0.54 and 1.05 Ω, respectively. A symmetric supercapacitor assembled with VC-39 had an energy density of 87.6 Wh kg^{-1} at a power density of 497 W kg^{-1} that decreased to 20.4 Wh kg^{-1} at a power density of 3272 W kg^{-1}. Saravanakumar et al. controlled the ratio of N-doped mesoporous carbon (N-MPC) nanospheres to V_2O_5 to obtain a superior supercapacitor electrode with maximum porosity [132]. The VC material comprised V_2O_5 flakes anchored onto the spherical N-MPC. These V_2O_5 covered carbon spheres formed agglomerations with other VC nanospheres. The hydrothermal method oxidized V_2O_5 to form pure orthorhombic crystals, while reducing the carbon into a graphitic crystal phase. A low N-MPC loading of 10% (VC-10) resulted in many uncoated carbon spheres due to V_2O_5 agglomeration. This decreased the accessibility to V_2O_5 for surface ion intercalation. At 5 wt% N-MPC, the carbon nanospheres were homogeneously covered to maximize the pseudocapacitive capacity of V_2O_5 with an optimal surface area of 8.77 m^2 g^{-1}. The addition of 15 wt% N-MPC resulted in nanospheres that were completely coated by V_2O_5, decreasing the accessibility to N-MPC for a suboptimal surface area of 10.35 m^2 g^{-1}. At 10 wt% N-MPC, the carbon nanospheres were effectively covered to maximize the pseudocapacitive capacity of V_2O_5 with an optimal surface area of 8.77 m^2 g^{-1}. VC-10 exhibited the highest C_{sp} of 487 F g^{-1} at a current density of 0.5 A g^{-1}, which was 34% higher than that of bare V_2O_5. The increase in capacitance was caused by a significant increase in surface area from 5.64 to 8.77 m^2 g^{-1} and increased conductivity because of N-MPC. An asymmetric supercapacitor with the VC-10 electrode had an energy density of 12.8 Wh kg^1 at a power density of 317 W kg^{-1}. Kudo et al. added varying amounts of acetylene black to a V_2O_5 sol to create a suspension with acetone surfactant [133]. The Ni foam was subsequently submerged in the suspension and heated at 120 °C for 5 h. The resulting VC was comprised of spherical carbon cores with an uneven V_2O_5 outer layer coating. These nanospheres formed bumpy agglomerations, yielding a BET surface area of 30 m^2 g^{-1}. With a large carbon content (30 wt% acetylene black), the VC exhibited good rate capability, maintaining a charge capacity of 340 mAh g^{-1} at a high current density of 54 A g^{-1}. The VC electrode maintained 100% of its capacity even after 2000 cycles at a charge rate of 20 C because the porosity of the VC material allowed unobstructed Li ion insertion/de-insertion. The maximum energy density was 80 Wh kg^{-1} at a power density of 26,000 W kg^{-1} with an average working voltage of 2 V, which rapidly deteriorated with repeated cycles. The average energy density was 15–20 Wh kg^{-1}. Peng et al. followed a similar synthesis route using Ketjen black powder and a V_2O_5 sol [134]. Ni foam was used as a template for VC coating. The VC material comprised V_2O_5 nanosheets covered with carbon nanospheres uniformly distributed on the hydrated V_2O_5 surface. An increase in the initial Ketjen black loading increased the final surface area of VC, with a maximum BET surface area of 264.72 m^2 g^{-1} for VC$_1$ (1 g Ketjen black loading). VC$_{0.5}$ (0.5 g Ketjen black loading) exhibited the highest C_{sp} of 1634 F g^{-1} at a current density of 5 mA cm^{-2} because of effective synergy between carbon for fast electron mobility and V_2O_5 nanosheets for high pseudocapacitance. A symmetric supercapacitor with the VC$_{0.5}$ electrodes had an energy density of 56.83 Wh kg^{-1} at a power density of 303 W kg^{-1}, which decreased slightly to 30.86 Wh kg^{-1} at a power density of 2433 W kg^{-1}. Despite not having a lower surface area and containing less conductive carbon content than VC$_1$, VC$_{0.5}$ retained a good rate capability while sustaining a high energy storage capacity.

5.3. Effects of Physical Treatment

Heat treatment of a VC composite can alter the morphology of the hybrid material [135]. Kim et al. synthesized VC by heating a mixture of vanadium trichloride, terephthalic acid, and DI water in an autoclave at 200 °C for four days. Subsequently, the VC powder was calcinated at 400 °C for 6 h in an argon atmosphere [136]. Prior to calcination, the VC exhibited a rectangular structure with large crystals that were 1–4 µm in length.

The heat-treated VC had a highly orthorhombic crystal structure with thinner nanorods that were 0.5–3 μm in length. A 4–6-nm-thick layer of graphitic carbon coated the V_2O_5 nanorods. The annealed VC exhibited an initial discharge rate of 286 mAh g^{-1} at 0.1 C, which was close to the theoretical limit of 294 mAh g^{-1}. Zhang et al. also analyzed the effects of annealing temperature and duration on the morphology of the VC material [137]. The VC composite was synthesized via a hydrothermal method and was further heat treated in a muffle furnace at varying temperatures of 300 to 500 °C for different durations in air. The hydrothermal synthesis yielded smooth prism-like monoclinic V_2O_5 protrusions with amorphous carbon nanospheres embedded between the V_2O_5 crystals. Calcination under air resulted in porous V_2O_5 nanoparticles with uneven surfaces due to combustion reactions with air. At a low calcination temperature of 300 °C, many carbon nanospheres remained scattered within the V_2O_5 nanorods, whereas no nanospheres were present in the VC that was heat treated at 500 °C. The presence of carbon nanospheres indicated the incomplete oxidation of V_2O_5, resulting in a lower C_{sp} of 151 F g^{-1} at a current density of 1 A g^{-1} for VC-300 compared to 367 F g^{-1} for VC-500. An increase in the calcination duration up to 8 h increased the C_{sp} of the VC composite because V_2O_5 had more time to nucleate. However, further increasing the calcination time to 12 h decreased the C_{sp} because the agglomeration of V_2O_5 resulted in limited surface ion diffusion.

Heat treatment can also promote the oxidation of V^{4+} to V^{5+} for a more crystalline V_2O_5. Zeiger et al. fabricated vanadium carbide/carbide core/shell composites (VC-C) by reacting vanadium carbide with $NiCl_2$ in a graphite crucible at 700 °C in chlorine gas followed by calcination at 450 °C in synthetic air to promote further oxidation of V^{4+} [138]. The resulting VC-C nanostructure was composed of a V_2O_5 core and carbide-derived carbon shell. Increasing the calcination temperature to 600 °C increased V_2O_5 oxidation but burned off most of the carbon shell. VC-C-90 (90% theoretically converted) exhibited the highest specific capacity of 415 mAh g^{-1} at a current density of 0.01 A g^{-1} with almost 100% coulombic efficiency. The partial conversion of the V_2O_5 core from vanadium carbide provided a large storage capacity, while the outer carbon shell increased the conductivity of the composite. A decrease in the annealing temperature to decrease the carbide shell burnoff while effectively oxidizing the vanadium carbide core was essential for maximum yield. An asymmetric supercapacitor setup with the VC-C-90 negative electrode yielded an energy density of 90 Wh kg^{-1} for charging and 50 Wh kg^{-1} for discharging at a power density of 166 W kg^{-1}. The energy density decreased to 27 Wh kg^{-1} at a high-power density of 6700 W kg^{-1}, retaining 80% of its energy density after 10,000 cycles at a current density of 1 A g^{-1}. Narayanan et al. annealed glucose-based VC at temperatures of 250–400 °C in air [139]. The composite contained thin V_2O_5 nanorods with CQDs anchored to the nanorods; the V_2O_5 nanorods also had a thin carbon coating. Increasing the annealing temperature decreased the thickness of the V_2O_5 nanorods and promoted V_2O_5 oxidation using oxygen from the atmosphere, resulting in more orthorhombic V_2O_5 crystals. VC annealed at 250 °C (VC250) exhibited the highest C_{sp} of 260 F g^{-1} at a current density of 1 A g^{-1}. The layered V_2O_5 crystal structure improved electron propagation, and the high surface area of the VC material increased the surface adsorption. VC250 also exhibited the lowest charge transfer resistance of 11.4 Ω. The VC250 electrode exhibited high cycling capability, retaining 92% of its C_{sp} after 5000 cycles at a current density of 5 A g^{-1} because the carbon coating decreased vanadium dissolution. The imperfections in the V_2O_5 lattice caused by V^{4+} enhanced the Li-ion intercalation capability and decreased V_2O_5 dissolution.

The heat treatment of VC composites can change the morphology of the composite and promote the oxidation of vanadium oxide to V_2O_5. Thus, controlling the annealing temperature and duration allows the formation of partially oxidized VC materials for increased stability and surface ion intercalation. However, excessive annealing temperatures and durations disintegrate the carbon content, resulting in a low conductivity. Therefore, it is essential to optimize both the annealing temperature and duration.

6. Conclusions

The synthesis of various metal oxide and carbon composites as supercapacitor electrode materials has attracted significant attention because of the increasing demand for high energy and power-dense energy storage devices used in portable electronics and electric vehicles. The development of stable vanadium oxide-based electrode materials has been extensively investigated due to the high energy storage potential and natural abundance of vanadium oxide. Common carbon nanostructures such as rGO, CNTs, CNFs, and CQDs have been combined with V_2O_5 to yield high-performance supercapacitor electrode materials.

V_2O_5/rGO composites can be synthesized using many methods, including hydro/solvothermal, sol-gel, filtration, and chemical deposition methods. These strategies often yield a lamellar rGO nanostructure with V_2O_5 intercalated between the nanosheets. V_2O_5/CNT hybrid materials are frequently synthesized as vertically aligned nanotubes infiltrated by V_2O_5 crystals or long nanotubes with V_2O_5 growth using various synthesis methods. The CNTs have the advantage of facile functionalization with hydroxyl or carboxyl groups to increase V_2O_5 nucleation and conductivity. The V_2O_5/CNF composites offer the unique advantage of having a highly stable 3D macrostructure that can be used as a template for the fabrication of free-standing and binderless electrodes. Using electrodeposition, crystallization, sol-dipping, or electrospinning methods, a fibrous structure with a CNF/V_2O_5 core/shell nanostructure or V_2O_5 crystals intercalated into web-like CNFs can be synthesized. Other V_2O_5/carbon materials such as CQD-based and amorphous carbon-flake-based composites can be easily synthesized via facile strategies such as the hydro/solvothermal method. Carbon precursors can be sourced from both artificially synthesized and bio-based carbonaceous materials.

In most cases, an increase in the V_2O_5 content in the V_2O_5/carbon hybrid materials increases the total energy storage potential because of faradic redox reactions. However, a high V_2O_5 content results in agglomerations that hinder surface ion adsorption. An increase in the carbon content leads to increased EDL contributions and conductivity for improved rate capability and cyclic stability. However, the low energy storage potential of carbon nanomaterials limits high carbon content for energy-dense electrode materials. An optimal balance of V_2O_5 and carbon can increase the surface area and porosity beyond that of solely the carbon material alone, enabling more activation sites for greater ion intercalation/de-intercalation. The synergy between V_2O_5 and carbon can also inhibit vanadium ion dissolution, resulting in a more stable charge/discharge. Physical treatment via annealing, calcination, and laser treatment can promote vanadium oxide oxidation to V_2O_5, altering the crystallinity of the hybrid material for improved electrochemical performance.

This review discusses the effects of different synthesis methods, V_2O_5/carbon compositions, and physical treatment strategies on the morphology and electrochemical performances of V_2O_5/carbon composites. This review is expected to serve as a catalyst for further research for the development of an ideal supercapacitor electrode material with high power and energy properties. Furthermore, light, solid-state supercapacitors based on V_2O_5/carbon nanomaterials have potential applications for portable, stretchable and wearable electronics. Continued research efforts in this area could make great contribution to developing supercapacitor technologies.

References

1. Najib, S.; Erdem, E. Current progress achieved in novel materials for supercapacitor electrodes: Mini review. *Nanoscale Adv.* **2019**, *1*, 2817–2827. [CrossRef]
2. Zhang, S.; Pan, N. Supercapacitors Performance Evaluation. *Adv. Energy Mater.* **2015**, *5*, 1401401. [CrossRef]
3. Simon, P.; Gogotsi, Y.; Dunn, B. Where do batteries end and supercapacitors begin? *Science* **2014**, *343*, 1210–1211. [CrossRef]
4. Lin, T.; Chen, I.W.; Liu, F.; Yang, C.; Bi, H.; Xu, F.; Huang, F. Nitrogen-doped mesoporous carbon of extraordinary capacitance for electrochemical energy storage. *Science* **2015**, *350*, 1508–1513. [CrossRef]
5. Vlad, A.; Singh, N.; Rolland, J.; Melinte, S.; Ajayan, P.M.; Gohy, J.F. Hybrid supercapacitor-battery materials for fast electrochemical charge storage. *Sci. Rep.* **2014**, *4*, 4315. [CrossRef]
6. Suganya, B.; Maruthamuthu, S.; Chandrasekaran, J.; Saravanakumar, B.; Vijayakumar, E.; Marnadu, R.; Al-Enizi, A.M.; Ubaidullah, M. Design of zinc vanadate ($Zn_3V_2O_8$)/nitrogen doped multiwall carbon nanotubes (N-MWCNT) towards supercapacitor electrode applications. *J. Electroanal. Chem.* **2021**, *881*, 114936. [CrossRef]
7. Patel, R.; Inamdar, A.I.; Hou, B.; Cha, S.N.; Ansari, A.T.; Gunjakar, J.L.; Im, H.; Kim, H. Solvothermal synthesis of high-performance Ni-Co layered double hydroxide nanofoam electrode for electrochemical energy storage. *Curr. Appl. Phys.* **2017**, *17*, 501–506. [CrossRef]
8. Zhu, J.; Chen, S.; Zhou, H.; Wang, X. Fabrication of a low defect density graphene-nickel hydroxide nanosheet hybrid with enhanced electrochemical performance. *Nano Res.* **2012**, *5*, 11–19. [CrossRef]
9. Nandi, D.; Mohan, V.B.; Bhowmick, A.K.; Bhattacharyya, D. Metal/metal oxide decorated graphene synthesis and application as supercapacitor: A review. *J. Mater. Sci.* **2020**, *55*, 6375–6400. [CrossRef]
10. Mathis, T.S.; Kurra, N.; Wang, X.; Pinto, D.; Simon, P.; Gogotsi, Y. Energy Storage Data Reporting in Perspective—Guidelines for Interpreting the Performance of Electrochemical Energy Storage Systems. *Adv. Energy Mater.* **2019**, *9*, 1902007. [CrossRef]
11. Iro, Z.S.; Subramani, C.; Dash, S.S. Electrochemical science: A brief review on electrode materials for supercapacitor. *Int. J. Electrochem. Sci.* **2016**, *11*, 10628–10643. [CrossRef]
12. Majumdar, D.; Mandal, M.; Bhattacharya, S.K. V_2O_5 and its Carbon-Based Nanocomposites for Supercapacitor Applications. *ChemElectroChem* **2019**, *6*, 1623–1648. [CrossRef]
13. Borenstein, A.; Hanna, O.; Attias, R.; Luski, S.; Brousse, T.; Aurbach, D. Carbon-based composite materials for supercapacitor electrodes: A review. *J. Mater. Chem. A* **2017**, *5*, 12653–12672. [CrossRef]
14. Ho, M.Y.; Khiew, P.S.; Isa, D.; Tan, T.K.; Chiu, W.S.; Chia, C.H. A review of metal oxide composite electrode materials for electrochemical capacitors. *Nano* **2014**, *9*, 1430002. [CrossRef]
15. Zhu, J.; Cao, L.; Wu, Y.; Gong, Y.; Liu, Z.; Hoster, H.E.; Zhang, Y.; Zhang, S.; Yang, S.; Yan, Q.; et al. Building 3D structures of vanadium pentoxide nanosheets and application as electrodes in supercapacitors. *Nano Lett.* **2013**, *13*, 5408–5413. [CrossRef] [PubMed]
16. Qian, A.; Pang, Y.; Wang, G.; Hao, Y.; Liu, Y.; Shi, H.; Chung, C.H.; Du, Z.; Cheng, F. Pseudocapacitive Charge Storage in MXene-V_2O_5 for Asymmetric Flexible Energy Storage Devices. *ACS Appl. Mater. Interfaces* **2020**, *12*, 54791–54797. [CrossRef] [PubMed]
17. Zhi, M.; Xiang, C.; Li, J.; Li, M.; Wu, N. Nanostructured carbon-metal oxide composite electrodes for supercapacitors: A review. *Nanoscale* **2013**, *5*, 72–88. [CrossRef] [PubMed]
18. Qu, Q.; Zhu, Y.; Gao, X.; Wu, Y. Core-Shell Structure of Polypyrrole Grown on V_2O_5 Nanoribbon as High Performance Anode Material for Supercapacitors. *Adv. Energy Mater.* **2012**, *2*, 950–955. [CrossRef]
19. Augustyn, V.; Simon, P.; Dunn, B. Pseudocapacitive oxide materials for high-rate electrochemical energy storage. *Energy Environ. Sci.* **2014**, *7*, 1597–1614. [CrossRef]
20. Chalker, C.J.; An, H.; Zavala, J.; Parija, A.; Banerjee, S.; Lutkenhaus, J.L.; Batteas, J.D. Fabrication and Electrochemical Performance of Structured Mesoscale Open Shell V_2O_5 Networks. *Langmuir* **2017**, *33*, 5975–5981. [CrossRef]
21. Gerbaldi, C.; Destro, M.; Nair, J.R.; Ferrari, S.; Quinzeni, I.; Quartarone, E. High-rate V_2O_5-based Li-ion thin film polymer cell with outstanding long-term cyclability. *Nano Energy* **2013**, *2*, 1279–1286. [CrossRef]
22. Mjejri, I.; Manceriu, L.M.; Gaudon, M.; Rougier, A.; Sediri, F. Nano-vanadium pentoxide films for electrochromic displays. *Solid State Ionics* **2016**, *292*, 8–14. [CrossRef]
23. Liu, Y.; Jia, C.; Wan, Z.; Weng, X.; Xie, J.; Deng, L. Electrochemical and electrochromic properties of novel nanoporous NiO/V_2O_5 hybrid film. *Sol. Energy Mater. Sol. Cells* **2015**, *132*, 467–475. [CrossRef]
24. Karade, S.S.; Lalwani, S.; Eum, J.H.; Kim, H. Coin cell fabricated symmetric supercapacitor device of two-steps synthesized V_2O_5 Nanorods. *J. Electroanal. Chem.* **2020**, *864*, 114080. [CrossRef]
25. Zhang, H.; Han, X.; Gan, R.; Guo, Z.; Ni, Y.; Zhang, L. A facile biotemplate-assisted synthesis of mesoporous V_2O_5 microtubules for high performance asymmetric supercapacitors. *Appl. Surf. Sci.* **2020**, *511*, 145527. [CrossRef]
26. Li, H.; Tian, H.; Chang, T.H.; Zhang, J.; Koh, S.N.; Wang, X.; Wang, C.H.; Chen, P.Y. High-Purity V_2O_5 Nanosheets Synthesized from Gasification Waste: Flexible Energy Storage Devices and Environmental Assessment. *ACS Sustain. Chem. Eng.* **2019**, *7*, 12474–12484. [CrossRef]
27. Zhang, S.; Chen, S.; Luo, Y.; Yan, B.; Gu, Y.; Yang, F.; Cao, Y. Large-scale preparation of solution-processable one-dimensional V_2O_5 nanobelts with ultrahigh aspect ratio for bifunctional multicolor electrochromic and supercapacitor applications. *J. Alloys Compd.* **2020**, *842*, 155882. [CrossRef]

28. Lee, H.; Kumbhar, V.S.; Lee, J.; Choi, Y.; Lee, K. Highly reversible crystal transformation of anodized porous V_2O_5 nanostructures for wide potential window high-performance supercapacitors. *Electrochim. Acta* **2020**, *334*, 135618. [CrossRef]

29. Uma Shankar, V.; Govindarajan, D.; Christuraj, P.; Salethraj, M.J.; Johanson, F.J.; Raja, M.D. Enhanced the electrochemical properties of Ni doped V_2O_5 as a electrode material for supercapacitor applications. In *Materials Today: Proceedings*; Elsevier BV: Amsterdam, The Netherlands, 2020.

30. Hsiao, Y.S.; Chang-Jian, C.W.; Syu, W.L.; Yen, S.C.; Huang, J.H.; Weng, H.C.; Lu, C.Z.; Hsu, S.C. Enhanced electrochromic performance of carbon-coated V_2O_5 derived from a metal–organic framework. *Appl. Surf. Sci.* **2021**, *542*, 148498. [CrossRef]

31. Ke, Q.; Wang, J. Graphene-based materials for supercapacitor electrodes–A review. *J. Mater.* **2016**, *2*, 37–54. [CrossRef]

32. Thalji, M.R.; Ali, G.A.M.; Lee, S.P.; Chong, K.F. Solvothermal Synthesis of Reduced Graphene Oxide as Electrode Material for Supercapacitor Application. *Chem. Adv. Mater.* **2019**, *4*, 17–26.

33. Yang, Z.; Tian, J.; Yin, Z.; Cui, C.; Qian, W.; Wei, F. Carbon nanotube- and graphene-based nanomaterials and applications in high-voltage supercapacitor: A review. *Carbon* **2019**, *141*, 467–480. [CrossRef]

34. Faraji, S.; Ani, F.N. The development supercapacitor from activated carbon by electroless plating–A review. *Renew. Sustain. Energy Rev.* **2015**, *42*, 823–834. [CrossRef]

35. Cottineau, T.; Toupin, M.; Delahaye, T.; Brousse, T.; Bélanger, D. Nanostructured transition metal oxides for aqueous hybrid electrochemical supercapacitors. *Appl. Phys. A Mater. Sci. Process.* **2006**, *82*, 599–606. [CrossRef]

36. Patel, R.; Park, J.T.; Patel, M.; Dash, J.K.; Gowd, E.B.; Karpoormath, R.; Mishra, A.; Kwak, J.; Kim, J.H. Transition-metal-based layered double hydroxides tailored for energy conversion and storage. *J. Mater. Chem. A* **2017**, *6*, 12–29. [CrossRef]

37. Noked, M.; Avraham, E.; Bohadana, Y.; Soffer, A.; Aurbach, D. Development of anion stereoselective, activated carbon molecular sieve electrodes prepared by chemical vapor deposition. *J. Phys. Chem. C* **2009**, *113*, 7316–7321. [CrossRef]

38. Xu, Y.; Lin, Z.; Zhong, X.; Huang, X.; Weiss, N.O.; Huang, Y.; Duan, X. Holey graphene frameworks for highly efficient capacitive energy storage. *Nat. Commun.* **2014**, *5*, 4554. [CrossRef]

39. Cheng, J.; Gu, G.; Guan, Q.; Razal, J.M.; Wang, Z.; Li, X.; Wang, B. Synthesis of a porous sheet-like V_2O_5-CNT nanocomposite using an ice-templating "bricks-and-mortar" assembly approach as a high-capacity, long cyclelife cathode material for lithium-ion batteries. *J. Mater. Chem. A* **2016**, *4*, 2729–2737. [CrossRef]

40. Mohd Abdah, M.A.A.; Azman, N.H.N.; Kulandaivalu, S.; Sulaiman, Y. Review of the use of transition-metal-oxide and conducting polymer-based fibres for high-performance supercapacitors. *Mater. Des.* **2020**, *186*, 108199. [CrossRef]

41. González, A.; Goikolea, E.; Barrena, J.A.; Mysyk, R. Review on supercapacitors: Technologies and materials. *Renew. Sustain. Energy Rev.* **2016**, *58*, 1189–1206. [CrossRef]

42. Delbari, S.A.; Ghadimi, L.S.; Hadi, R.; Farhoudian, S.; Nedaei, M.; Babapoor, A.; Sabahi Namini, A.; Van Le, Q.; Shokouhimehr, M.; Shahedi Asl, M.; et al. Transition metal oxide-based electrode materials for flexible supercapacitors: A review. *J. Alloys Compd.* **2021**, *857*, 158281. [CrossRef]

43. Kumar, K.S.; Choudhary, N.; Jung, Y.; Thomas, J. Recent Advances in Two-Dimensional Nanomaterials for Supercapacitor Electrode Applications. *ACS Energy Lett.* **2018**, *3*, 482–495. [CrossRef]

44. Raghavendra, K.V.G.; Vinoth, R.; Zeb, K.; Muralee Gopi, C.V.V.; Sambasivam, S.; Kummara, M.R.; Obaidat, I.M.; Kim, H.J. An intuitive review of supercapacitors with recent progress and novel device applications. *J. Energy Storage* **2020**, *31*, 101652. [CrossRef]

45. Lokhande, V.C.; Lokhande, A.C.; Lokhande, C.D.; Kim, J.H.; Ji, T. Supercapacitive composite metal oxide electrodes formed with carbon, metal oxides and conducting polymers. *J. Alloys Compd.* **2016**, *682*, 381–403. [CrossRef]

46. Dubey, R.; Guruviah, V. Review of carbon-based electrode materials for supercapacitor energy storage. *Ionics* **2019**, *25*, 1419–1445. [CrossRef]

47. Fisher, R.A.; Watt, M.R.; Jud Ready, W. Functionalized Carbon Nanotube Supercapacitor Electrodes: A Review on Pseudocapacitive Materials. *ECS J. Solid State Sci. Technol.* **2013**, *2*, M3170–M3177. [CrossRef]

48. Bose, S.; Kuila, T.; Mishra, A.K.; Rajasekar, R.; Kim, N.H.; Lee, J.H. Carbon-based nanostructured materials and their composites as supercapacitor electrodes. *J. Mater. Chem.* **2012**, *22*, 767–784. [CrossRef]

49. Perera, S.D.; Liyanage, A.D.; Nijem, N.; Ferraris, J.P.; Chabal, Y.J.; Balkus, K.J. Vanadium oxide nanowire-Graphene binder free nanocomposite paper electrodes for supercapacitors: A facile green approach. *J. Power Sources* **2013**, *230*, 130–137. [CrossRef]

50. Ding, B.; Guo, D.; Wang, Y.; Wu, X.; Fan, Z. Functionalized graphene nanosheets decorated on carbon nanotubes networks for high performance supercapacitors. *J. Power Sources* **2018**, *398*, 113–119. [CrossRef]

51. Ding, B.; Wu, X. Transition metal oxides anchored on graphene/carbon nanotubes conductive network as both the negative and positive electrodes for asymmetric supercapacitor. *J. Alloys Compd.* **2020**, *842*, 155838. [CrossRef]

52. Chem, J.M.; Tarcan, R.; Todor-boer, O.; Petrovai, I.; Leordean, C. Reduced graphene oxide today. *J. Mater. Chem. C* **2019**, *8*, 1198–1224.

53. Patil, S.J.; Chodankar, N.R.; Han, Y.K.; Lee, D.W. Carbon alternative pseudocapacitive V_2O_5 nanobricks and δ-MnO_2 nanoflakes@α-MnO_2 nanowires hetero-phase for high-energy pseudocapacitor. *J. Power Sources* **2020**, *453*, 227766. [CrossRef]

54. Pandey, G.P.; Liu, T.; Brown, E.; Yang, Y.; Li, Y.; Sun, X.S.; Fang, Y.; Li, J. Mesoporous Hybrids of Reduced Graphene Oxide and Vanadium Pentoxide for Enhanced Performance in Lithium-Ion Batteries and Electrochemical Capacitors. *ACS Appl. Mater. Interfaces* **2016**, *8*, 9200–9210. [CrossRef] [PubMed]

55. Ahirrao, D.J.; Mohanapriya, K.; Jha, N. V_2O_5 nanowires-graphene composite as an outstanding electrode material for high electrochemical performance and long-cycle-life supercapacitor. *Mater. Res. Bull.* **2018**, *108*, 73–82. [CrossRef]

56. Geng, Z.D.; Wang, Y.-P. Synthesis of $V_2O_5 \cdot 1.6H_2O$/graphene composite and its application in supercapacitors. *J. Solid State Electrochem.* **2015**, *19*, 3131–3138. [CrossRef]

57. Sun, W.; Gao, G.; Du, Y.; Zhang, K.; Wu, G. A facile strategy for fabricating hierarchical nanocomposites of V_2O_5 nanowire arrays on a three-dimensional N-doped graphene aerogel with a synergistic effect for supercapacitors. *J. Mater. Chem. A* **2018**, *6*, 9938–9947. [CrossRef]

58. Nagaraju, D.H.; Wang, Q.; Beaujuge, P.; Alshareef, H.N. Two-dimensional heterostructures of V_2O_5 and reduced graphene oxide as electrodes for high energy density asymmetric supercapacitors. *J. Mater. Chem. A* **2014**, *2*, 17146–17152. [CrossRef]

59. Sahu, V.; Goel, S.; Kumar Tomar, A.; Singh, G.; Sharma, R.K. Graphene Nanoribbons @ Vanadium Oxide Nanostrips for Supercapacitive Energy Storage. *Electrochim. Acta* **2017**, *230*, 255–264. [CrossRef]

60. Zhang, H.; Xie, A.; Wang, C.; Wang, H.; Shen, Y.; Tian, X. Bifunctional reduced graphene oxide/V_2O_5 composite hydrogel: Fabrication, high performance as electromagnetic wave absorbent and supercapacitor. *ChemPhysChem* **2014**, *15*, 366–373. [CrossRef]

61. Tabatabai Yazdi, S.; Mousavi, M.; Khorrami, G.H. Effect of Co-doping in V_2O_5 nanoparticles synthesized via a gelatin-based sol-gel method. *Mater. Today Commun.* **2021**, *26*, 101955. [CrossRef]

62. Yilmaz, G.; Lu, X.; Ho, G.W. Cross-linker mediated formation of sulfur-functionalized V_2O_5/graphene aerogels and their enhanced pseudocapacitive performance. *Nanoscale* **2017**, *9*, 802–811. [CrossRef] [PubMed]

63. Kiruthiga, R.; Nithya, C.; Karvembu, R.; Venkata Rami Reddy, B. Reduced Graphene Oxide Embedded V_2O_5 Nanorods and Porous Honey Carbon as High Performance Electrodes for Hybrid Sodium-ion Supercapacitors. *Electrochim. Acta* **2017**, *256*, 221–231.

64. Wang, L.; Shu, T.; Guo, S.; Lu, Y.; Li, M.; Nzabahimana, J.; Hu, X. Fabricating strongly coupled V_2O_5@PEDOT nanobelts/graphene hybrid films with high areal capacitance and facile transferability for transparent solid-state supercapacitors. *Energy Storage Mater.* **2020**, *27*, 150–158. [CrossRef]

65. Liu, H.; Tang, Y.; Wang, C.; Xu, Z.; Yang, C.; Huang, T.; Zhang, F.; Wu, D.; Feng, X. A Lyotropic Liquid-Crystal-Based Assembly Avenue toward Highly Oriented Vanadium Pentoxide/Graphene Films for Flexible Energy Storage. *Adv. Funct. Mater.* **2017**, *27*, 1606269. [CrossRef]

66. Foo, C.Y.; Sumboja, A.; Tan, D.J.H.; Wang, J.; Lee, P.S. Flexible and highly scalable V_2O_5-rGO electrodes in an organic electrolyte for supercapacitor devices. *Adv. Energy Mater.* **2014**, *4*, 1400236. [CrossRef]

67. Van Hoa, N.; Quyen, T.T.H.; Nghia, N.H.; Van Hieu, N.; Shim, J.J. In situ growth of flower-like V_2O_5 arrays on graphene@nickel foam as high-performance electrode for supercapacitors. *J. Alloys Compd.* **2017**, *702*, 693–699. [CrossRef]

68. Wang, A.Y.; Chaudhary, M.; Lin, T.W. Enhancing the stability and capacitance of vanadium oxide nanoribbons/3D-graphene binder-free electrode by using $VOSO_4$ as redox-active electrolyte. *Chem. Eng. J.* **2019**, *355*, 830–839. [CrossRef]

69. Korkmaz, S.; Tezel, F.M.; Kariper, A. Synthesis and Characterization of GO/V_2O_5 Thin Film Supercapacitor. *Synth. Met.* **2018**, *242*, 37–48. [CrossRef]

70. Li, G.; Wang, X.; Hassan, F.M.; Li, M.; Batmaz, R.; Xiao, X.; Yu, A. Vanadium Pentoxide Nanorods Anchored to and Wrapped with Graphene Nanosheets for High-Power Asymmetric Supercapacitors. *ChemElectroChem* **2015**, *2*, 1264–1269. [CrossRef]

71. Saravanakumar, B.; Purushothaman, K.K.; Muralidharan, G. Fabrication of two-dimensional reduced graphene oxide supported V_2O_5 networks and their application in supercapacitors. *Mater. Chem. Phys.* **2016**, *170*, 266–275. [CrossRef]

72. Ramadoss, A.; Saravanakumar, B.; Kim, S.J. Vanadium Pentoxide/Reduced Graphene Oxide Composite as an Efficient Electrode Material for High-Performance Supercapacitors and Self-Powered Systems. *Energy Technol.* **2015**, *3*, 913–924. [CrossRef]

73. Lee, M.; Balasingam, S.K.; Jeong, H.Y.; Hong, W.G.; Lee, H.B.R.; Kim, B.H.; Jun, Y. One-step hydrothermal synthesis of Graphene decorated V_2O_5 nanobelts for enhanced electrochemical energy storage. *Sci. Rep.* **2015**, *5*, srep08151. [CrossRef] [PubMed]

74. Fu, M.; Zhuang, Q.; Zhu, Z.; Zhang, Z.; Chen, W.; Liu, Q.; Yu, H. Facile synthesis of V_2O_5/graphene composites as advanced electrode materials in supercapacitors. *J. Alloys Compd.* **2021**, *862*, 158006. [CrossRef]

75. Yao, L.; Zhang, C.; Hu, N.; Zhang, L.; Zhou, Z.; Zhang, Y. Three-dimensional skeleton networks of reduced graphene oxide nanosheets/vanadium pentoxide nanobelts hybrid for high-performance supercapacitors. *Electrochim. Acta* **2019**, *295*, 14–21. [CrossRef]

76. Choudhury, A.; Bonso, J.S.; Wunch, M.; Yang, K.S.; Ferraris, J.P.; Yang, D.J. In-situ synthesis of vanadium pentoxide nanofibre/exfoliated graphene nanohybrid and its supercapacitor applications. *J. Power Sources* **2015**, *287*, 283–290. [CrossRef]

77. Deng, L.; Gao, Y.; Ma, Z.; Fan, G. Free-standing graphene/vanadium oxide composite as binder-free electrode for asymmetrical supercapacitor. *J. Colloid Interface Sci.* **2017**, *505*, 556–565. [CrossRef]

78. Ndiaye, N.M.; Ngom, B.D.; Sylla, N.F.; Masikhwa, T.M.; Madito, M.J.; Momodu, D.; Ntsoane, T.; Manyala, N. Three dimensional vanadium pentoxide/graphene foam composite as positive electrode for high performance asymmetric electrochemical supercapacitor. *J. Colloid Interface Sci.* **2018**, *532*, 395–406. [CrossRef]

79. Li, M.; Sun, G.; Yin, P.; Ruan, C.; Ai, K. Controlling the formation of rodlike V_2O_5 nanocrystals on reduced graphene oxide for high-performance supercapacitors. *ACS Appl. Mater. Interfaces* **2013**, *5*, 11462–11470. [CrossRef]

80. Liu, Z.; Zhang, H.; Yang, Q.; Chen, Y. Graphene/V_2O_5 hybrid electrode for an asymmetric supercapacitor with high energy density in an organic electrolyte. *Electrochim. Acta* **2018**, *287*, 149–157. [CrossRef]

81. Thangappan, R.; Kalaiselvam, S.; Elayaperumal, A.; Jayavel, R. Synthesis of graphene oxide/vanadium pentoxide composite nanofibers by electrospinning for supercapacitor applications. *Solid State Ionics* **2014**, *268*, 321–325. [CrossRef]

82. Lee, S.M.; Park, Y.J.; Van Lam, D.; Kim, J.H.; Lee, K. Effects of annealing on electrochemical performance in graphene/V_2O_5 supercapacitor. *Appl. Surf. Sci.* **2020**, *512*, 145626. [CrossRef]

83. Lazauskas, A.; Marcinauskas, L.; Andrulevicius, M. Modification of Graphene Oxide/$V_2O_5 \cdot nH_2O$ Nanocomposite Films via Direct Laser Irradiation. *ACS Appl. Mater. Interfaces* **2020**, *12*, 18877–18884. [CrossRef] [PubMed]

84. Zhu, S.; Ni, J.; Li, Y. Carbon nanotube-based electrodes for flexible supercapacitors. *Nano Res.* **2020**, *13*, 1825–1841. [CrossRef]

85. Kumar, S.; Saeed, G.; Zhu, L.; Hui, K.N.; Kim, N.H.; Lee, J.H. 0D to 3D carbon-based networks combined with pseudocapacitive electrode material for high energy density supercapacitor: A review. *Chem. Eng. J.* **2021**, *403*, 126352. [CrossRef]

86. Lin, Z.; Yan, X.; Lang, J.; Wang, R.; Kong, L. Bin Adjusting electrode initial potential to obtain high-performance asymmetric supercapacitor based on porous vanadium pentoxide nanotubes and activated carbon nanorods. *J. Power Sources* **2015**, *279*, 358–364. [CrossRef]

87. Wallar, C.J.; Poon, R.; Zhitomirsky, I. High Areal Capacitance of V_2O_3–Carbon Nanotube Electrodes. *J. Electrochem. Soc.* **2017**, *164*, A3620–A3627. [CrossRef]

88. Jiang, H.; Cai, X.; Qian, Y.; Zhang, C.; Zhou, L.; Liu, W.; Li, B.; Lai, L.; Huang, W. V_2O_5 embedded in vertically aligned carbon nanotube arrays as free-standing electrodes for flexible supercapacitors. *J. Mater. Chem. A* **2017**, *5*, 23727–23736. [CrossRef]

89. Wang, X.; Zuo, C.; Jia, L.; Liu, Q.; Guo, X.; Jing, X.; Wang, J. Synthesis of sandwich-like vanadium pentoxide/carbon nanotubes composites for high performance supercapacitor electrodes. *J. Alloys Compd.* **2017**, *708*, 134–140. [CrossRef]

90. Jampani, P.H.; Velikokhatnyi, O.; Kadakia, K.; Hong, D.H.; Damle, S.S.; Poston, J.A.; Manivannan, A.; Kumta, P.N. High energy density titanium doped-vanadium oxide-vertically aligned CNT composite electrodes for supercapacitor applications. *J. Mater. Chem. A* **2015**, *3*, 8413–8432. [CrossRef]

91. Shakir, I.; Ali, Z.; Bae, J.; Park, J.; Kang, D.J. Layer by layer assembly of ultrathin V_2O_5 anchored MWCNTs and graphene on textile fabrics for fabrication of high energy density flexible supercapacitor electrodes. *Nanoscale* **2014**, *6*, 4125–4130. [CrossRef]

92. Hu, T.; Liu, Y.; Zhang, Y.; Chen, M.; Zheng, J.; Tang, J.; Meng, C. 3D hierarchical porous $V_3O_7 \cdot H_2O$ nanobelts/CNT/reduced graphene oxide integrated composite with synergistic effect for supercapacitors with high capacitance and long cycling life. *J. Colloid Interface Sci.* **2018**, *531*, 382–393. [CrossRef]

93. Mtz-enriquez, A.I.; Gomez-solis, C.; Oliva, A.I.; Zakhidov, A.; Martinez, P.M.; Garcia, C.R.; Herrera-ramirez, A.; Oliva, J. Enhancing the voltage and discharge times of graphene supercapacitors depositing a CNT/V_2O_5 layer on their electrodes. *Mater. Chem. Phys.* **2020**, *244*, 122698. [CrossRef]

94. Saravanakumar, B.; Purushothaman, K.K.; Muralidharan, G. V_2O_5/functionalized MWCNT hybrid nanocomposite: The fabrication and its enhanced supercapacitive performance. *RSC Adv.* **2014**, *4*, 37437–37445. [CrossRef]

95. Pandit, B.; Dubal, D.P.; Gómez-Romero, P.; Kale, B.B.; Sankapal, B.R. V_2O_5 encapsulated MWCNTs in 2D surface architecture: Complete solid-state bendable highly stabilized energy efficient supercapacitor device. *Sci. Rep.* **2017**, *7*, srep43430. [CrossRef]

96. Guo, K.; Li, Y.; Li, C.; Yu, N.; Li, H. Compact self-standing layered film assembled by $V_2O_5 nH_2O$/CNTs 2D/1D composites for high volumetric capacitance flexible supercapacitors. *Sci. China Mater.* **2019**, *62*, 936–946. [CrossRef]

97. Yilmaz, G.; Guo, C.X.; Lu, X. High-Performance Solid-State Supercapacitors Based on V_2O_5/Carbon Nanotube Composites. *ChemElectroChem* **2016**, *3*, 158–164. [CrossRef]

98. Wu, J.; Gao, X.; Yu, H.; Ding, T.; Yan, Y.; Yao, B.; Yao, X.; Chen, D.; Liu, M.; Huang, L. A Scalable Free-Standing V_2O_5/CNT Film Electrode for Supercapacitors with a Wide Operation Voltage (1.6 V) in an Aqueous Electrolyte. *Adv. Funct. Mater.* **2016**, *26*, 6114–6120. [CrossRef]

99. Perera, S.D.; Patel, B.; Nijem, N.; Roodenko, K.; Seitz, O.; Ferraris, J.P.; Chabal, Y.J.; Balkus, K.J. Vanadium oxide nanowire-carbon nanotube binder-free flexible electrodes for supercapacitors. *Adv. Energy Mater.* **2011**, *1*, 936–945. [CrossRef]

100. Sathiya, M.; Prakash, A.S.; Ramesha, K.; Tarascon, J.M.; Shukla, A.K. V_2O_5-anchored carbon nanotubes for enhanced electrochemical energy storage. *J. Am. Chem. Soc.* **2011**, *133*, 16291–16299. [CrossRef] [PubMed]

101. Sun, G.; Ren, H.; Shi, Z.; Zhang, L.; Wang, Z.; Zhan, K.; Yan, Y.; Yang, J.; Zhao, B. V_2O_5/vertically-aligned carbon nanotubes as negative electrode for asymmetric supercapacitor in neutral aqueous electrolyte. *J. Colloid Interface Sci.* **2021**, *588*, 847–856. [CrossRef] [PubMed]

102. Wang, Q.; Zou, Y.; Xiang, C.; Chu, H.; Zhang, H.; Xu, F.; Sun, L.; Tang, C. High-performance supercapacitor based on V_2O_5/carbon nanotubes-super activated carbon ternary composite. *Ceram. Int.* **2016**, *42*, 12129–12135. [CrossRef]

103. Shakir, I.; Choi, J.H.; Shahid, M.; Shahid, S.A.; Rana, U.A.; Sarfraz, M.; Kang, D.J. Ultra-thin and uniform coating of vanadium oxide on multiwall carbon nanotubes through solution based approach for high-performance electrochemical supercapacitors. *Electrochim. Acta* **2013**, *111*, 400–404. [CrossRef]

104. Zhou, X.; Wang, Y.; Gong, C.; Liu, B.; Wei, G. Production, structural design, functional control, and broad applications of carbon nanofiber-based nanomaterials: A comprehensive review. *Chem. Eng. J.* **2020**, *402*, 126189. [CrossRef]

105. Adam, A.A.; Dennis, J.O.; Al-Hadeethi, Y.; Mkawi, E.M.; Abdulkadir, B.A.; Usman, F.; Hassan, Y.M.; Wadi, I.A.; Sani, M. State of the art and new directions on electrospun lignin/cellulose nanofibers for supercapacitor application: A systematic literature review. *Polymers* **2020**, *12*, 2884. [CrossRef] [PubMed]

106. Song, Y.; Liu, T.Y.; Yao, B.; Kou, T.Y.; Feng, D.Y.; Liu, X.X.; Li, Y. Amorphous Mixed-Valence Vanadium Oxide/Exfoliated Carbon Cloth Structure Shows a Record High Cycling Stability. *Small* **2017**, *13*, 1700067. [CrossRef]

107. Zhou, X.; Chen, Q.; Wang, A.; Xu, J.; Wu, S.; Shen, J. Bamboo-like Composites of V_2O_5/Polyindole and Activated Carbon Cloth as Electrodes for All-Solid-State Flexible Asymmetric Supercapacitors. *ACS Appl. Mater. Interfaces* **2016**, *8*, 3776–3783. [CrossRef]
108. Azadian, F.; Rastogi, A.C. V_2O_5 Film Embedded Carbon Fiber Paper Synthesized by Sol Process as Highly Pseudocapacitive Electrode for Energy Storage. *ECS Meet. Abstr.* **2020**, *97*, 25.
109. Zhou, X.; Gao, X.; Liu, M.; Wang, C.; Chu, F. Synthesis of 3D phosphorus doped graphene foam in carbon cloth to support V_2O_5/CoMoS$_4$ hybrid for flexible all-solid-state asymmetry supercapacitors. *J. Power Sources* **2020**, *453*, 227902. [CrossRef]
110. Xiao, Y.; Xu, Y.; Zhang, K.; Tang, X.; Huang, J.; Yuan, K.; Chen, Y. Coaxial electrospun free-standing and mechanical stable hierarchical porous carbon nanofiber membrane for flexible supercapacitors. *Carbon* **2020**, *160*, 80–87. [CrossRef]
111. Wang, H.; Niu, H.; Wang, H.; Wang, W.; Jin, X.; Wang, H.; Zhou, H.; Lin, T. Micro-meso porous structured carbon nanofibers with ultra-high surface area and large supercapacitor electrode capacitance. *J. Power Sources* **2021**, *482*, 228986. [CrossRef]
112. Kim, B.H.; Kim, C.H.; Yang, K.S.; Rahy, A.; Yang, D.J. Electrospun vanadium pentoxide/carbon nanofiber composites for supercapacitor electrodes. *Electrochim. Acta* **2012**, *83*, 335–340. [CrossRef]
113. Kim, B.H.; Yang, K.S.; Yang, D.J. Electrochemical behavior of activated carbon nanofiber-vanadium pentoxide composites for double-layer capacitors. *Electrochim. Acta* **2013**, *109*, 859–865. [CrossRef]
114. Choudhury, A.; Kim, J.; Yang, K.; Yang, D. Electrochimica Acta Facile synthesis of self-standing binder-free vanadium pentoxide-carbon nano fi ber composites for high-performance supercapacitors. *Electrochim. Acta* **2016**, *213*, 400–407. [CrossRef]
115. Velayutham, R.; Manikandan, R.; Raj, C.J.; Kale, A.M.; Kaya, C.; Palanisamy, K.; Kim, B.C. Electrodeposition of vanadium pentoxide on carbon fiber cloth as a binder-free electrode for high-performance asymmetric supercapacitor. *J. Alloys Compd.* **2021**, *863*, 158332. [CrossRef]
116. Chen, S.; Jiang, H.; Cheng, Q.; Wang, G.; Petr, S.; Li, C. Amorphous vanadium oxides with metallic character for asymmetric supercapacitors. *Chem. Eng. J.* **2021**, *403*, 126380. [CrossRef]
117. You, M.; Zhang, W.; Yan, X.; Jiang, H.; Miao, J.; Li, Y.; Zhou, W.; Zhu, Y.; Cheng, X. V_2O_5 nanosheets assembled on 3D carbon fiber felt as a free-standing electrode for flexible asymmetric supercapacitor with remarkable energy density. *Ceram. Int.* **2021**, *47*, 3337–3345. [CrossRef]
118. Guo, Y.; Li, J.; Chen, M.; Gao, G. Facile synthesis of vanadium pentoxide@carbon core-shell nanowires for high-performance supercapacitors. *J. Power Sources* **2015**, *273*, 804–809. [CrossRef]
119. Sun, W.; Gao, G.; Zhang, K.; Liu, Y.; Wu, G. Self-assembled 3D N-CNFs/V_2O_5 aerogels with core/shell nanostructures through vacancies control and seeds growth as an outstanding supercapacitor electrode material. *Carbon* **2018**, *132*, 667–677. [CrossRef]
120. Parmar, R.; Neto, D.D.F.; Matsubara, E.Y.; Gunnella, R.; Rosolen, J.M. Electrochemical synthesis and structural characterization of nanostructured $V_2O_5.nH_2O$ on CNTs coated/uncoated carbon felt composite. *Nano-Struct. Nano-Objects* **2020**, *24*, 100538. [CrossRef]
121. Panigrahi, K.; Howli, P.; Chattopadhyay, K.K. 3D network of V_2O_5 for flexible symmetric supercapacitor. *Electrochim. Acta* **2020**, *337*, 135701. [CrossRef]
122. Zhu, Z.; Xu, Z. The rational design of biomass-derived carbon materials towards next-generation energy storage: A review. *Renew. Sustain. Energy Rev.* **2020**, *134*, 110308. [CrossRef]
123. Daubert, J.S.; Lewis, N.P.; Gotsch, H.N.; Mundy, J.Z.; Monroe, D.N.; Dickey, E.C.; Losego, M.D.; Parsons, G.N. Effect of Meso- and Micro-Porosity in Carbon Electrodes on Atomic Layer Deposition of Pseudocapacitive V_2O_5 for High Performance Supercapacitors. *Chem. Mater.* **2015**, *27*, 6524–6534. [CrossRef]
124. Zhang, Y.; Zheng, J.; Wang, Q.; Zhang, S.; Hu, T.; Meng, C. One-step hydrothermal preparation of $(NH_4)2V_3O_8$/carbon composites and conversion to porous V_2O_5 nanoparticles as supercapacitor electrode with excellent pseudocapacitive capability. *Appl. Surf. Sci.* **2017**, *423*, 728–742. [CrossRef]
125. Narayanan, R. Single step hydrothermal synthesis of carbon nanodot decorated V_2O_5 nanobelts as hybrid conducting material for supercapacitor application. *J. Solid State Chem.* **2017**, *253*, 103–112. [CrossRef]
126. Sethuraman, B.; Kamatchi Kamaraj, P. Carbon Coated Flowery V_2O_5 Nanostructure as Novel Electrode Material for High Performance Supercapacitors. *Electrochim. Acta* **2015**, *186*, 285–291.
127. Ngom, B.D.; Ndiaye, N.M.; Sylla, N.F.; Mutuma, B.K.; Manyala, N. Sustainable development of vanadium pentoxide carbon composites derived from: Hibiscus sabdariffa family for application in supercapacitors. *Sustain. Energy Fuels* **2020**, *4*, 4814–4830. [CrossRef]
128. Mei, J.; Ma, Y.; Pei, C. V_2O_5 nanobelt-carbonized bacterial cellulose composite with enhanced electrochemical performance for aqueous supercapacitors. *J. Solid State Electrochem.* **2017**, *21*, 573–580. [CrossRef]
129. Fleischmann, S.; Zeiger, M.; Jäckel, N.; Krüner, B.; Lemkova, V.; Widmaier, M.; Presser, V. Tuning pseudocapacitive and battery-like lithium intercalation in vanadium dioxide/carbon onion hybrids for asymmetric supercapacitor anodes. *J. Mater. Chem. A* **2017**, *5*, 13039–13051. [CrossRef]
130. Zhang, G.; Ren, L.; Hu, D.; Zhang, S.; Gu, H. Fabrication of mesoporous carbon hollow spheres intercalated three-dimensional network structure V_2O_5 nanosheets with enhanced electrochemical performance. *J. Alloys Compd.* **2019**, *781*, 407–414. [CrossRef]
131. Zhu, C.; Hu, D.; Liu, Z. Interconnected three-dimensionally hierarchical heterostructures with homogeneously-dispersed V_2O_5 nanocrystals and carbon for high performance supercapacitor electrodes. *Electrochim. Acta* **2017**, *229*, 155–165. [CrossRef]
132. Saravanakumar, B.; Purushothaman, K.K.; Muralidharan, G. V_2O_5/nitrogen enriched mesoporous carbon spheres nanocomposite as supercapacitor electrode. *Microporous Mesoporous Mater.* **2018**, *258*, 83–94. [CrossRef]

133. Kudo, T.; Ikeda, Y.; Watanabe, T.; Hibino, M.; Miyayama, M.; Abe, H.; Kajita, K. Amorphous V_2O_5/carbon composites as electrochemical supercapacitor electrodes. *Solid State Ionics* **2002**, *152–153*, 833–841. [CrossRef]

134. Peng, T.; Wang, J.; Liu, Q.; Liu, J.; Wang, P. Mesoporous V_2O_5/Ketjin black nanocomposites for all-solid-state symmetric supercapacitors. *CrystEngComm* **2015**, *17*, 1673–1679. [CrossRef]

135. Xing, L.L.; Zhao, G.G.; Huang, K.J.; Wu, X. A yolk-shell V_2O_5 structure assembled from ultrathin nanosheets and coralline-shaped carbon as advanced electrodes for a high-performance asymmetric supercapacitor. *Dalt. Trans.* **2018**, *47*, 2256–2265. [CrossRef] [PubMed]

136. Kim, T.; Kim, H.; You, T.S.; Kim, J. Carbon-coated V_2O_5 nanoparticles derived from metal-organic frameworks as a cathode material for rechargeable lithium-ion batteries. *J. Alloys Compd.* **2017**, *727*, 522–530. [CrossRef]

137. Zhang, Y.; Zheng, J.; Wang, Q.; Hu, T.; Meng, C. Hydrothermal synthesis of vanadium dioxides/carbon composites and their transformation to surface-uneven V_2O_5 nanoparticles with high electrochemical properties. *RSC Adv.* **2016**, *6*, 93741–93752. [CrossRef]

138. Zeiger, M.; Ariyanto, T.; Krüner, B.; Peter, N.J.; Fleischmann, S.; Etzold, B.J.M.; Presser, V. Vanadium pentoxide/carbide-derived carbon core-shell hybrid particles for high performance electrochemical energy storage. *J. Mater. Chem. A* **2016**, *4*, 18899–18909. [CrossRef]

139. Narayanan, R.; Dewan, A.; Chakraborty, D. Complimentary effects of annealing temperature on optimal tuning of functionalized carbon-V_2O_5 hybrid nanobelts for targeted dual applications in electrochromic and supercapacitor devices. *RSC Adv.* **2018**, *8*, 8596–8606. [CrossRef]